Inorganic Chemistry

pubs.acs.org/IC

Article

Acoustic Shock Wave-Induced Solid-State Fusion of Nanoparticles: A Case Study of the Conversion of One-Dimensional Rod Shape into Three-Dimensional Honeycomb Nanostructures of CdO for High-Performance Energy Storage Materials

Sivakumar Aswathappa, Lidong Dai,* S. Sahaya Jude Dhas, S. A. Martin Britto Dhas, Sourav Laha, Raju Suresh Kumar, and Abdulrahman I. Almansour

Cite This: *Inorg. Chem.* 2024, 63, 576−592

Read Online

ACCESS | Metrics & More | Article Recommendations | Supporting Information

ABSTRACT: Herein, we describe the solid-state fusion of rod-shaped to honeycomb-shaped cadmium oxide particles (CdO NPs) caused by the process of repeated exposure to acoustic shock waves. Significant changes have been observed in structurally and morphologically dependent properties. For instance, at the 200-shocked condition, the high-pressure CdO-B2 phase is present as a secondary phase wherein all of the rod-shaped particles have been transformed into honeycomb-shaped CdO particles which possess comparatively higher specific-capacitance than CdO nanorods (NRs). The computed specific capacitance values for the 0, 100, and 200 shocked samples at a scan rate of 100 m V s^{-1} are computed to be 433, 415, and 583 F g^{-1}, respectively. The second-stage decomposition temperature points of the CdO NPs have significantly increased in accordance with the morphological changes from rod to honeycomb patterns such that the values are 343, 526, and 534 °C, respectively, for 0, 100, and 200 shocked conditions. Note that such honeycomb nanostructured CdO particles by shock-wave processing have never been observed, to date. Due to the superior energy storage abilities as well as the spectacular high thermal stability of the honeycomb CdO nanostructures compared to CdO NRs, shocked CdO with honeycomb nanostructures can be considered as energy storage materials.

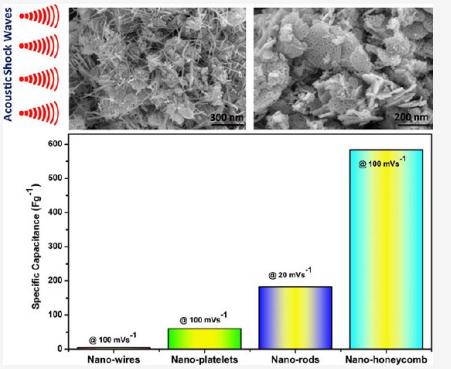

1. INTRODUCTION

Searching for new materials with the desired properties has become a state-of-the-art endeavor, with which several new crystals and nanostructures keep pouring into the mainstream. Novel nanostructured materials have the potential to open new directions in materials research, possessing enhanced and exotic functional properties.[1−3] It is generally acknowledged that when particles enter the nano regime, their size and shape rather than their original crystal structure become the crucial factors that alter the properties of the nanomaterial significantly. Particle morphology has been regarded as a more significant criterion than particle size since the modified aspects of surface chemistry can make it possible to tailor nanostructures to the required applications.[4−6]

Apart from the conventional methods for creating nanoparticles,[7,8] a variety of unconventional routes, such as static high pressure,[9,10] laser shock waves,[11,12] gamma irradiations,[13,14] high energy ions irradiations,[15] electronic irradiations,[16] and acoustic shock waves,[17−20] can potentially be alternative methods for tailoring the aspects of surface chemistry of the nanoparticles. The crystal structure, size, and shape of nanoparticles are reported to have been altered by using the procedures indicated above. Hence, these routes may lead to the synthesis of a variety of novel nano forms with various multifunctional properties. The processing of the nanoparticles by static high pressure and laser shock waves has an extensive track record in recent decades.[9−12] However, the knowledge of how acoustic shock waves interact with nanomaterials is still at its formative level, and only a few articles have been published thus far.[21,22] Acoustic shock waves may have more influence on promoting nanostructures than laser shock waves and static high-pressure techniques despite the fact that there are many postprocessing technologies available for this purpose. The experimental outcomes of tabletop pressure-driven shock tubes have recently made it possible to analyze the characteristics of materials at pressures of several bars and temperatures of a few thousand Kelvin.[21,22] The dynamic recrystallization induced by shock waves leads to changes in morphology, magnetic phase shifts, material

Received: October 4, 2023
Revised: November 28, 2023
Accepted: November 30, 2023
Published: December 18, 2023

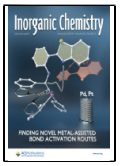

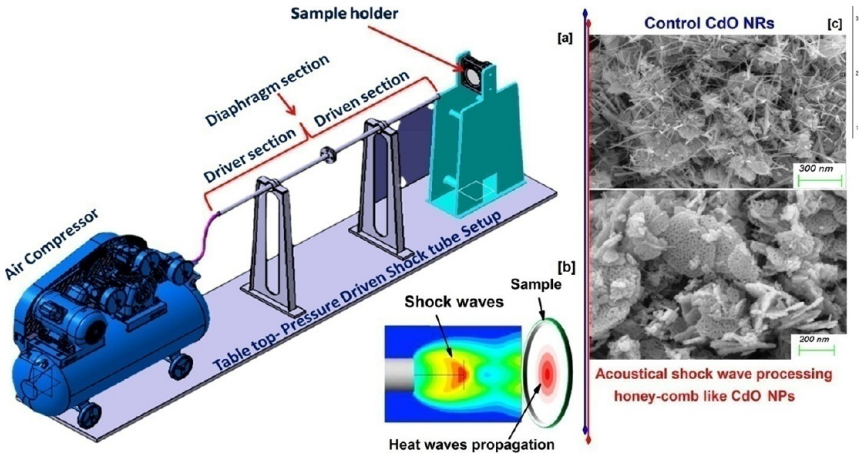

Figure 1. (a) Schematic diagram of the pressure driven shock tube (Reddy tube) experimental setup (b) shock wave propagation on the test sample. (c) FESEM images of the control and 200 shocked CdO NPs.

deformation, and electronic structure, crystallographic and molecular structural properties.[23−29] Only a few studies on technologically significant nanoparticles have been published thus far, but they have produced some intriguing findings such as crystallographic phase transitions (TiO_2, ZrO_2),[23,24] molecular phase transitions (α-Fe_2O_3, Co_3O_4),[25,26] magnetic phase transitions ($CoFe_2O_4$, $ZnFe_2O_4$),[27,28] crystalline to amorphous (SiO_2),[29] amorphous to crystalline (multiwall carbon nanotubes)[30] whereas, in some other cases, stable crystal structures and morphologies have been observed.[31,32] In addition to the structural aspects, a few interesting results have been observed in the electrochemical properties. For instance, in the case of MWCNTs, the specific capacitance for the control, 150 and 300 shocks-loaded CNTs are found to be 196, 215, and 294 F g^{-1}, respectively, at 100 mV s^{-1}.[30] Considering $CoFe_2O_4$ NPs,[33] the specific capacitance is observed to be 201, 355, 282, and 287 F g^{-1} for the control, 50, 100, and 150 shocked samples, respectively, at 100 mV s^{-1}, and similar kind of considerable changes have been found for the α-V_2O_5 NPs and $ZnFe_2O_4$ NPs under pre and postshocked conditions due to the subtle changes in the surface morphology.[34,35]

In the present work, we examined the effect of acoustic shock waves on the crystal structure and their surface morphological features of CdO NRs as well as their surface-dependent properties. The title NRs is one of the interesting oxide forms of materials and it has several applications especially, in semiconductor-based electronic devices including optoelectronic devices, gas-sensors, photosensors, transparent conductors, solar cells, high-density optical memories, visual displays, catalysts.[36−39] CdO can be crystallized in two crystallographic structures such as the NaCl type structure with the *F*m-3m space group (B1) and the CsCl type structure with the *P*m-3m space group (B2). The values of lattice parameters are $a = b = c = 4.77$ Å and $a = b = c = 2.94$ Å for the respective B1 and B2 CdO structures while the unit cell volumes are 27.15 and 25.41 $Å^3$. The B1 and B2 crystal structures are considered as the room temperature phase and high-pressure phase, while the B1 phase has 6-fold coordinated and B2 has 8-fold coordinated CsCl structures, respectively. Several high-pressure researchers have reported the phase transitions of B1 to B2 experimentally[40] as well as theoretically[41−46] and found the critical phase transition pressure value is ∼102 and ∼100 GPa, respectively. However, compared to the theoretical reports, experimental research on high-pressure behaviors on structural and surface-related properties is very limited for the CdO NPs. On the other hand, several nanoscience researchers have synthesized the B1 crystal structure CdO NPs with the adoption of different synthesis techniques and so far, several morphological CdO nanoparticles have been reported which are nanocubes,[47] nanospheres[48] nanobelts,[49] nanorods,[50] nanostrands,[51] nanowires,[52] nanoparticles,[53] spindles,[54] coconut fiber bark shaped CdO[54] and nanoflakes.[55] In addition, CdO undergoes significant changes in its energy storage efficiency with respect to its morphological features. In the previous report, Kumar et al. reported the specific capacitance of the rod-shaped CdO NPs[50] which is 183 F g^{-1} at 20 m V s^{-1}, while for the CdO nanowires[56] and nanoplatelets,[57] the reported values of specific capacitance are 5 and 60 at 100 mV s^{-1}, respectively. Based on the extensive literature reports, even though several morphological features have been reported for the CdO NPs, honeycomb-like morphological featured particles have not been reported, and such kind of morphological features have played a vital role in energy storage applications.

In the current work, we report the shock wave-induced self-assembly of honeycomb morphological CdO NPs which is the first report to date featuring the novel surface morphology of the title sample. Interestingly, the honeycomb morphological CdO NPs have higher electrical energy storage efficiency than traditional rod-shaped CdO.

2. EXPERIMENTAL SECTION

2.1. Synthesis of CdO NRs. All of the reagents were of analytical purity, such that they were used without any further purification. Deionized water was used throughout the synthesis process. To begin with, 10 mL of cadmium nitrate tetrahydrate aqueous solution ($Cd(NO_3)_2{\cdot}4H_2O$, 0.5 $molL^{-1}$) at room temperature was attained with vigorous agitation. The prepared solution was stirred for an hour, and subsequently, ammonia solution was added drop by drop until the prepared solution reached pH 8. While adding ammonia, a white precipitate was formed and stirring of the solution was continued for 5 h at room temperature. Then, the white precipitate was kept to settle down for 5 h. Thereafter, the solution was filtered and washed repeatedly with distilled water, ethanol, and distilled water to remove the unreacted materials. The obtained precipitate was dried at 80 °C for 10 h and then ground into a fine white powder with the help of a mortar and pestle. The resulting powder was calcinated at 500 °C for

https://doi.org/10.1021/acs.inorgchem.3c03461
Inorg. Chem. 2024, 63, 576−592

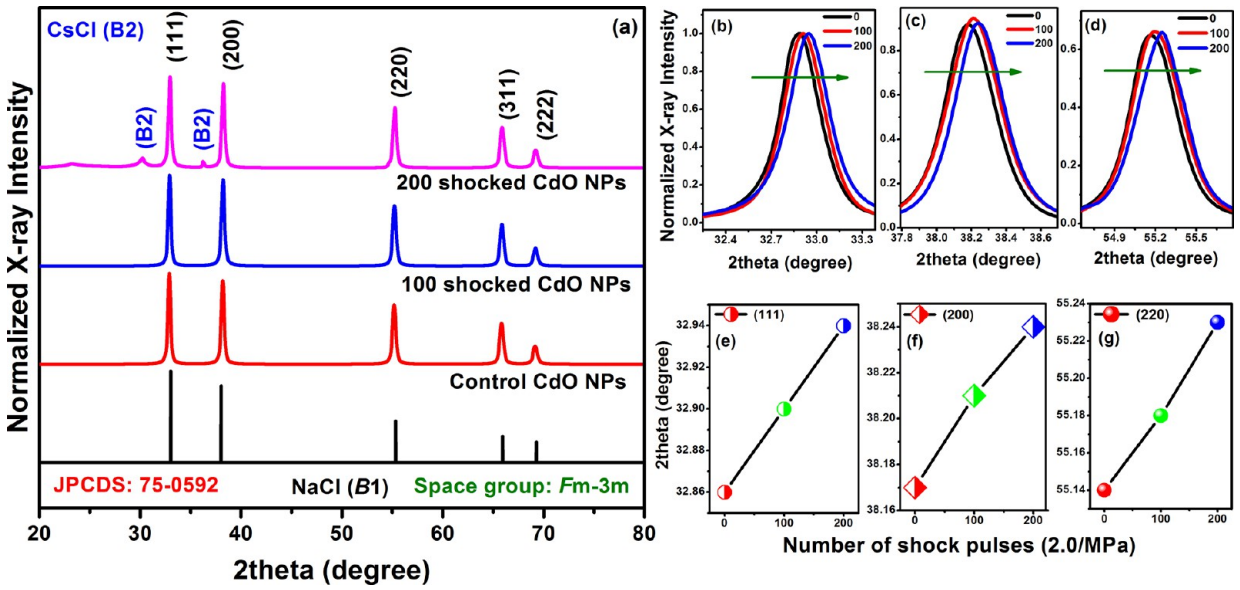

Figure 2. (a) XRD patterns of the control and shocked CdO NRs (b) zoomed-in version of the (111) plane, (c) zoomed-in version of the (200) plane, (d) zoomed-in version of the (220) plane, and (e) diffraction angle shift profiles of the (111) plane, (f) (200) and (g) (220) CdO NRs against the number of shock pulses.

3 h for obtaining the final product, which was utilized for further studies.

2.2. Shock Wave Loading Procedure. In the present experiment, a tabletop pressure-driven shock tube has been utilized and the details about the shock tube instrumentation as well as the shock wave-loading process have been discussed in the previous reports.[23,26] For the current study, we have chosen shock waves of Mach number 2.2 with transient pressure (P_5) and temperature (T_5) of 2.0 MPa and 864 K, respectively. In total, 3 equal amounts of samples have been chosen such that one sample has been kept as the control sample while the other two samples have been treated with 100 and 200 shocks, respectively. Figure 1a,b shows the schematic diagram of the experimental setup of the shock tube while Figure 1c shows the pre- and postshocked surface morphology of CdO NPs. A detailed discussion on the shock tube construction and shock wave loading procedure is provided in the Supplementary Section. After the completion of the shock wave-loading process, all the test samples have been sent for analytical measurements and functional property measurements such as optical, electrical, and electrochemical properties.

2.3. Instrumentation Details. The analysis of Powder X-ray diffraction (PXRD) analysis [Rigaku−Smart Lab X-ray Diffractometer, Japan-Cu Kα_1 as the X-ray source (λ = 1.5407 Å), with a step precision of ±0.001°] was performed. Ultraviolet diffused reflectance spectroscope (UV-DRS ShimadzuUV-3600 plus) has been utilized to understand linear optical properties. A vibrating sample magnetometer (Lake Shore, Cryotronics) was employed to understand the magnetic phase stability of the test samples under shocked conditions. A field emission scanning electron microscope (Carl Zeiss FESEM-Sigma 300, Schottky FEG) operating at the acceleration voltage of 10 kV was used to analyze the morphology of the title material. Microscopical structural characterizations for the starting and shock-recovered samples were investigated using an HRTEM, which was operated at the State Key Laboratory of Environmental Geochemistry, Institute of Geochemistry, Chinese Academy of Sciences, Guiyang, China. A small amount of the sample was homogeneously distributed onto a carbon-film-coated copper grid for the HRTEM observation, which was performed through a Tecnai G2 F20 S-TWIN TMP with an acceleration voltage of 200 kV. The interplanar spacing of the samples was precisely measured through Digital Micrograph software.

2.4. Electrochemical Measurement. An electrochemical workstation (SP-150, BioLogic Science Instruments, France) at ambient temperature was used for the present experiment. The working electrode has been prepared by bending 80 wt % of active material (CdO NRs), 10 wt % polyvinylidene fluoride (PVDF) binder with 0.3 mL of *N*-methylproline (NMP) solution, and 10 wt % conductive carbon black. The prepared uniform slurry has been painted onto precleaned 1 × 1 cm^2 nickel foam and allowed to air-dry for 24 h at ambient conditions. The above-mentioned method was used to fabricate the activated charcoal for the negative electrode as well. A three-electrode cell has been used for the measurement (electrolyte−3 mol KOH solution, working electrode−the prepared material, counter electrode−Pt wire, reference−Ag/AgCl in the saturated KCl). Shock wave-loaded sample electrodes of counts 50, 100, and 150 have been also prepared by employing the above-mentioned procedure. The cyclic voltammetry (CV) tests have been carried out for the control and postshocked samples for different applied potentials under the applied voltage ranging from 0 to 0.5 V. The asymmetric supercapacitor (ASC) has been assembled in a sandwich-type configuration using a CdO cathode, AC anode, and 3 M KOH electrolyte.

3. RESULTS AND DISCUSSION

3.1. Powder X-ray Diffraction Results. The powder-XRD patterns of the control and postshocked CdO NRs are presented in Figure 2a. As seen in Figure 2a, the control sample has five sharp and intense diffraction lines at 2θ = 32.90, 38.20, 55.20, 65.87, and 69.15°, respectively, such that the line positions are found to be well-matched with the B1 structure of CdO (JCPDS-75-0592)[49,50,58] and the corresponding diffraction planes are (111), (200), (220), (311) and (222), respectively. Note that, as seen in the XRD pattern of the control CdO NRs, it is clear that there is no notable signature for the formation of mixed-phase which is coupled with the high-pressure phase (B2) of CdO. At the 100 shock condition, the test sample retains its original crystal structure of the B1 phase and there is no change in the intensity ratio levels, but subtle changes are noted in the diffraction angle such that a shift toward the higher angle side can indicate the crystal structure which has undergone a slight lattice compression. Surprisingly, at the 200-shocked condition, there is a clear signature for the formation of the B2 phase of CdO as a secondary phase and the corresponding diffraction

https://doi.org/10.1021/acs.inorgchem.3c03461
Inorg. Chem. 2024, 63, 576−592

lines are at 30.21 and 36.23°, respectively.[40] Moreover, a continuous high-angle shift of the diffraction lines could be noticed at the 200-shocked condition which indicates the reduction of the B1-CdO lattice (Figure 2b−g). Note that, according to the static compression experiment, the pure B1 phase is highly stable up to 84.4 GPa at room temperature and up to the melting temperature (1427 °C) at ambient pressure.

The B2 phase starts at 90.06 GPa and the complete conversion of B1 to B2 takes place at 102.5 GPa.[40] The above-mentioned B1 to B2 phase transition occurs because of the sudden volume contraction of CdO and across the transition, the required volume reduction is approximately 6% i.e., from 27.15 to 25.41 Å^3. However, in the present acoustic shock wave processing experiment, the above-mentioned mixed phases of B1 and B2 could be obtained at 200 shock conditions with a transient pressure of 2.0 MPa. The shock transient pressure is much lower than that of the static pressure, which clearly demonstrates that the applied shock waves could produce more pronounced structural effects on CdO NRs than that of the static compression. The possible reason for such effects could be that the static compression experiments have been performed at room temperature and at high-pressure conditions[40] wherein pressure is the only leading catalyst to induce the phase transitions by causing the lattice compression. However, under shocked conditions, the transient pressure and temperature share almost an equal contribution to induce the structural transitions, and most importantly, in such experimental cases, thermal diffusivity and thermal conductivity parameters play a prominent role such that the low thermal transport ability of the material might have been largely affected by the impact of shock waves[59,60] as the thermal conductivity of CdO[61] is 8 Wm^{-1} K^{-1} which is almost seven times lower than ZnO (54 Wm^{-1} K^{-1}).[61,62] Because of the higher thermal energy dissipation ability, the shock wave temperature might not be sufficient to begin the recrystallization process within the shock wave propagation time scale, and hence, the crystal structure and microstructure of ZnO NRs are highly stable even up to 400 shocked conditions.[63,64] Due to the poor thermal transport ability of CdO NRs compared to ZnO NRs, the applied shock wave energy may provide sufficient latent heat energy to recrystallize the CdO structure whereby the higher phase of B2 occurs at the 200-shocked condition.

3.2. FE-SEM Analysis. In Figure 3, FE-SEM images of the control and shocked CdO NRs are presented. As witnessed in Figure 3a, in the control CdO NRs, most of the particles have rod-shaped morphologies, and also some of the particles are slightly agglomerated with irregular hexagonal-shaped particles.[50,55] At the 100 shock conditions, the density of the rod-shaped CdO particles is significantly reduced such that most of the rods are converted into shapeless particles, and the corresponding image is presented in Figure 3b. At the 200 shock conditions, the rodlike shape is almost nullified; thus, all the rods are converted into the honeycomb-shaped morphology with a hexagonal pattern, and the corresponding image is presented in Figure 3c.

The complete morphology feature of the CdO is because of the shock wave dynamic recrystallization process, which is highly associated with the thermal properties of the test sample. In addition to that, using conventional techniques, the synthesis of several nanostructures such as nanocubes,[48] nanospheres,[49] nanobelts,[50] nanorods,[51] nanostrands,[52] nanowires,[53] nanospindles,[54] nanococonut fiber bark-shaped CdO[54]

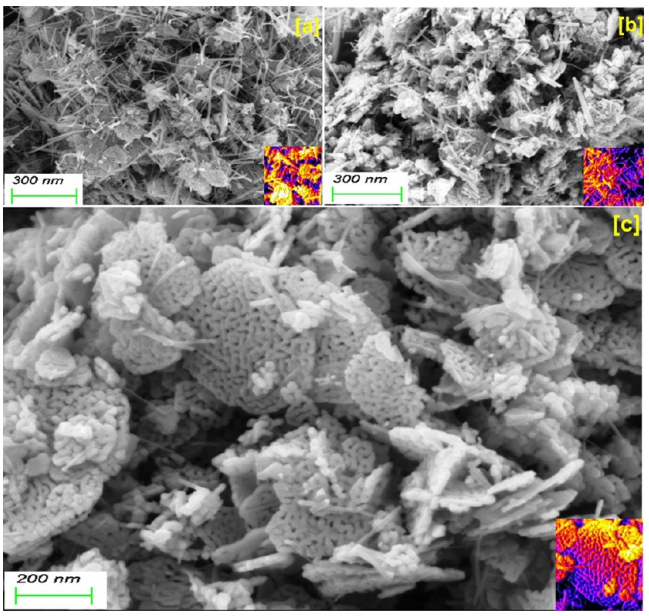

Figure 3. FE-SEM images of the control and shocked CdO NRs (a) control and (b) 100 and (c) 200 shocked CdO NRs.

and nanoflakes[55] have been accomplished and to the best of our knowledge, to date, there is no report found for the honeycomb surface morphological feature for the CdO NPs and this is the first observation of such novel nanostructured morphology for the CdO NPs for which images of better resolution are presented in Figure 4. Usually, the applied shock wave's transient pressure and temperature try to collapse the morphology thereby most of the NPs lose their original shape and undergo morphological deformations[11,12,25,26] whereas a few of the materials retain their original morphological features.[32] But constructively, tuning the morphology with required shape nanostructures under shocked conditions is

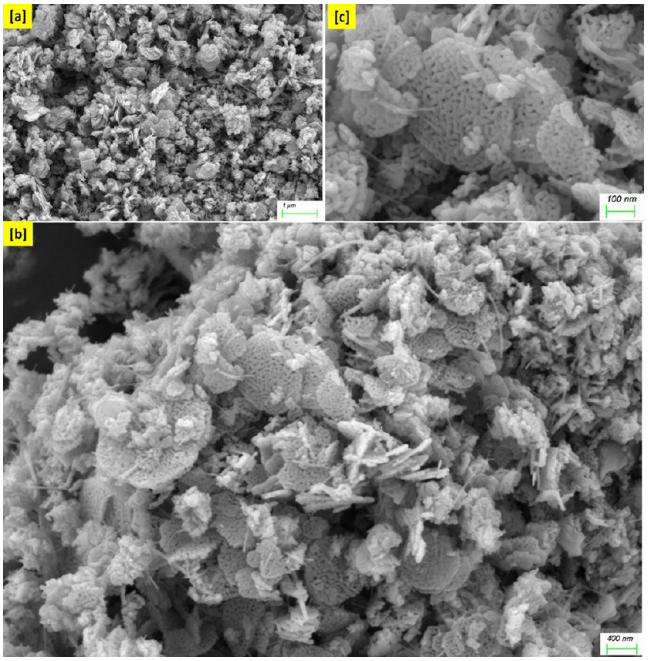

Figure 4. FE-SEM images of the 200 shocked CdO NPs (a) 1 μm (b) 400 nm (c) 100 nm.

https://doi.org/10.1021/acs.inorgchem.3c03461
Inorg. Chem. 2024, 63, 576−592

highly unknown as of now. As reflected in the XRD results, the ZnO and CdO NRs have large similarities in the structural point of view[42,61] and hence comparing their morphological stability under shocked conditions is quite relevant. Note that, in the case of ZnO NRs, there is no change noticed up to 200-shocked conditions due to the high structural stability as well as high thermal transport ability.[64] Hence, the applied shock wave temperature easily dissipates in the sample, such that no significant change is caused. However, in the present case, there is a chance of a temperature-associated tuning process in the morphological aspect because of the low thermal transport value, and hence the shock wave could contribute to the beginning of the recrystallization process by the thermal effect. Therefore, while increasing the number of shock pulses, the rod-shaped particles may break and transform into a honeycomb morphology (Figure 3c). Because of the sudden impact of the shock pulse of 2.0 M Pa and 864 K transient temperature on the test sample surface, it experiences the superheating effect within milliseconds; therefore, it undergoes the premelting process. Thus, the shocked solid is easily overheated above the melting line because the standard temperature-induced melting needs a long characteristic time. In addition to that, under shocked conditions (during the shock wave propagation), the test sample undergoes the premelting process which is referred to as the molten state.[65−67]

If the thermal diffusivity and conductivity parameters are low, the premelting process and molten state could produce more pronounced effects from the structural and morphological point of view.[59] Therefore, during the shocked conditions, the rod-shaped particles undergo the premelting state at the molten pool such that after the shock wave propagation, they are crystallized into the hexagonal-shaped honeycomb morphology. Because, the control CdO NPs have irregular hexagonal-shaped particles such that during the shock wave propagation, the molten state undergoes the solid-state conversion wherein the hexagonal morphology is the most probable and favorable morphology compared to the other shapes.[65−67] Hence, during the shock wave-induced dynamic recrystallization, the rods are converted into the hexagonal-shaped honeycomb morphology. In addition to that, as reflected in Figure 4b,c, the entire hexagonal-shaped honeycomb morphology is made up of several arrays of tiny CdO nanorods which are due to the fusion process influenced by the shock premelting process. The typical fusion process is referred to as the conversion from simple forms to complex forms as well as the conversion in terms of the physical density aspects. Here also, a similar concept is brought in such that the simple one-dimensional rod structures have been converted into complex three-dimensional structures by the impact of the shock wave-induced dynamic recrystallization. The process of nanorods formation or the sustainability of these rods under shocked conditions requires the lateral mass transport (thermal gradients) within the time scale of milliseconds and if the test sample cannot undergo such thermodynamic conditions, it may succumb to several changes such as induced chemical separations, surface reshaping, and phase segregations which are based on the unsteady thermodynamic state of the test sample.[65−67] Based on the abovementioned parameters, in the present case, phase segregations and significant surface reshaping are observed in the CdO at the 200-shocked condition.

3.3. High-Resolution Transmission Electron Microscopy Results. High-resolution transmission electron microscopy (HR-TEM) measurements have been performed to realize better the growth mechanism of the CdO NPs and to find the significant stable planes during the shocked conditions as well as to confirm the formation of the B2 phase at the 200-shocked state, such that the captured HR-TEM images are presented in Figure 5. The Moiré fringe pattern of the control

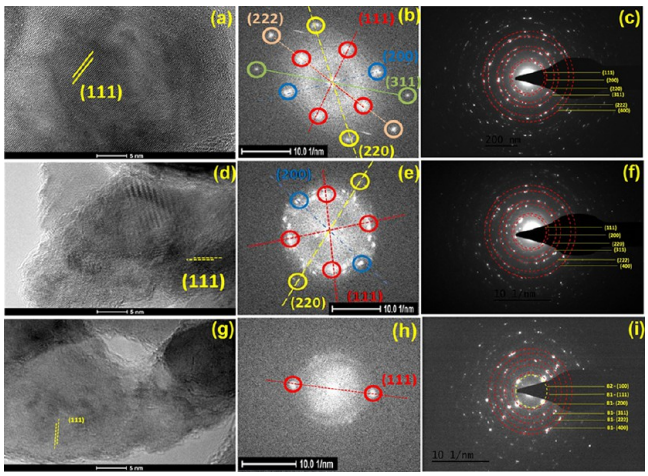

Figure 5. HR-TEM images of the control and shocked CdO (a) Moiré fringe pattern (b) FFT pattern (c) SAED pattern of the control CdO (d) Moiré fringe pattern (e) FFT pattern (f) SAED pattern of the 100 shocked CdO (g) Moiré fringe pattern (h) FFT pattern (i) SAED pattern of the 200 shocked CdO.

CdO NPs, the corresponding FFT pattern, and the SAED pattern are portrayed in Figure 5a−c. Figure 5a clearly represents the major and dominant crystalline plane of (111) without any visible defects and deformations even at the atomic level, which clearly implies that the control sample has a high degree of crystalline nature and it is identified to be well-matched with the XRD results.

The FFT pattern of the control CdO NRs (Figure 5b) shows the well-separated spots which are indexed with the B1 phase, and the indexed planes are (111), (200), (220), (222), and (311). The SAED pattern of the control sample (Figure 5c) also exhibits indexing lines similar to that of the FFT pattern, and the high-intensity electron diffraction dots highly support the consideration of the high degree of crystalline nature of the control sample. At the 100-shocked condition, considerable changes are noted especially in the Moiré fringe pattern and FFT pattern, and the corresponding images are displayed in Figure 5d−f. As seen in Figure 5d, it is quite clear that the 100-shocked CdO NPs have undergone considerable lattice stress and deformations, and the FFT pattern also supports this claim. Note that the well-separated FFT spots are changed into irregular patterns and intensities of high-angle diffraction lines which are also considerably reduced such that it is because of the enhancement of lattice stress and deformations followed by the lattice compression by the impact of shock waves, whereas, at the 200-shocked condition, only the (111) diffraction line is active in the FFT pattern (Figure 5h) which clearly represents the deformation levels that have massively increased due to the high transient pressure effects. In addition to that, Figure 5i shows the new SAED pattern ring at the lower angle diffraction, wherein the

https://doi.org/10.1021/acs.inorgchem.3c03461
Inorg. Chem. 2024, 63, 576−592

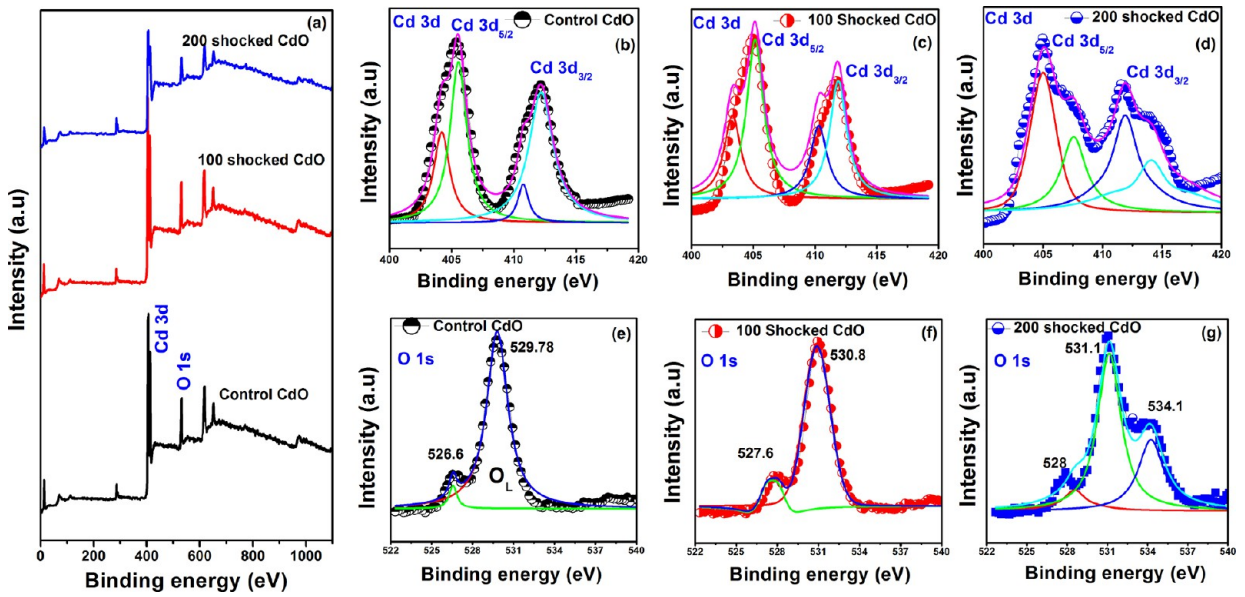

Figure 6. (a) Survey XPS spectra of the control and shocked CdO NPs, (b–d) Core Cd 3d spectra of the control, 100 and 200 shocked samples (e–g) Core O 1s spectra of the control, 100 and 200 shocked samples.

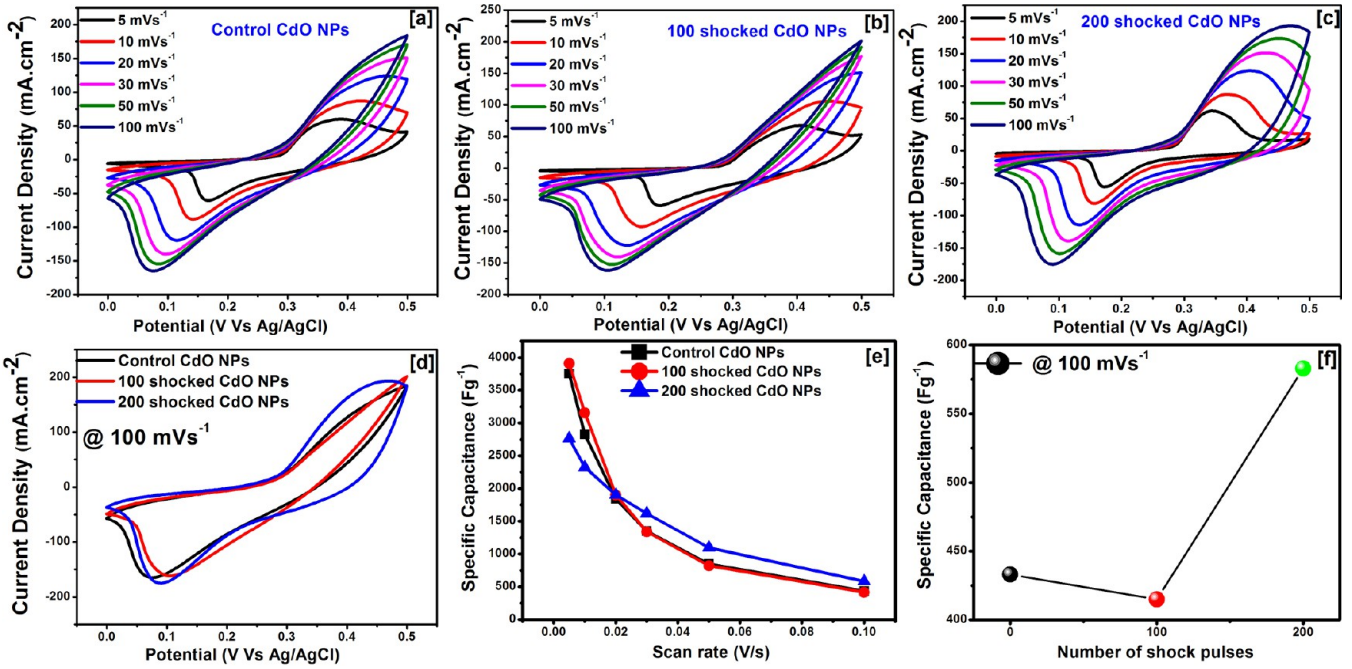

Figure 7. CV loops of the CdO NPs (a) control (b) 100 shocks (c) 200 shocks (d) comparison CV plots at 100 mV s^{-1} (e) scan rate vs specific capacitance (f) specific capacitance values at 100 mV s^{-1} with respect to the number of shock pulses

d-space value is identified to be well-matched with the B2 phase of the diffraction line (100) and the electron diffraction studies are in good agreement with the XRD results.

3.4. X-ray Photoelectron Spectroscopic Results. X-ray photoelectron spectroscopic (XPS) analysis was carried out to evaluate the original chemical structure and chemical states of the test samples of the control and under shocked conditions such that the obtained XPS spectra are presented in Figure 6. As seen in Figure 6b, the control sample's XPS spectrum has the spin–orbits Cd $3d_{3/2}$ and Cd $3d_{5/2}$, while O 1s spectrum exhibits main peaks at 405.50, 412.05, and 529.78 eV whereby the obtained values are found to be well-matched with the previous B1 phase CdO.[68,69] In addition to that, during the deconvolution process, the shoulder peaks in Cd $3d_{3/2}$ and Cd $3d_{5/2}$ orbitals may have arisen due to the adsorbed surface hydroxyl groups ($Cd(OH_2)$) such that the obtained results are found to be well corroborated with the literature. Moreover, the binding energy difference between the Cd $3d_{3/2}$ and Cd $3d_{5/2}$ orbital is found to be 6.55 eV which corresponds to the formation of the B1 phase of CdO.[68] While increasing the number of shock pulses, the lower binding energy shift of Cd $3d_{3/2}$ and Cd $3d_{5/2}$ could be found, which may be because of the formation of morphological changes occurring under shocked conditions. For example, at the 100 shock condition (Figure 6c), not much difference has been found in the peak shapes; however, the peaks have been shifted toward the lower

https://doi.org/10.1021/acs.inorgchem.3c03461
Inorg. Chem. 2024, 63, 576–592

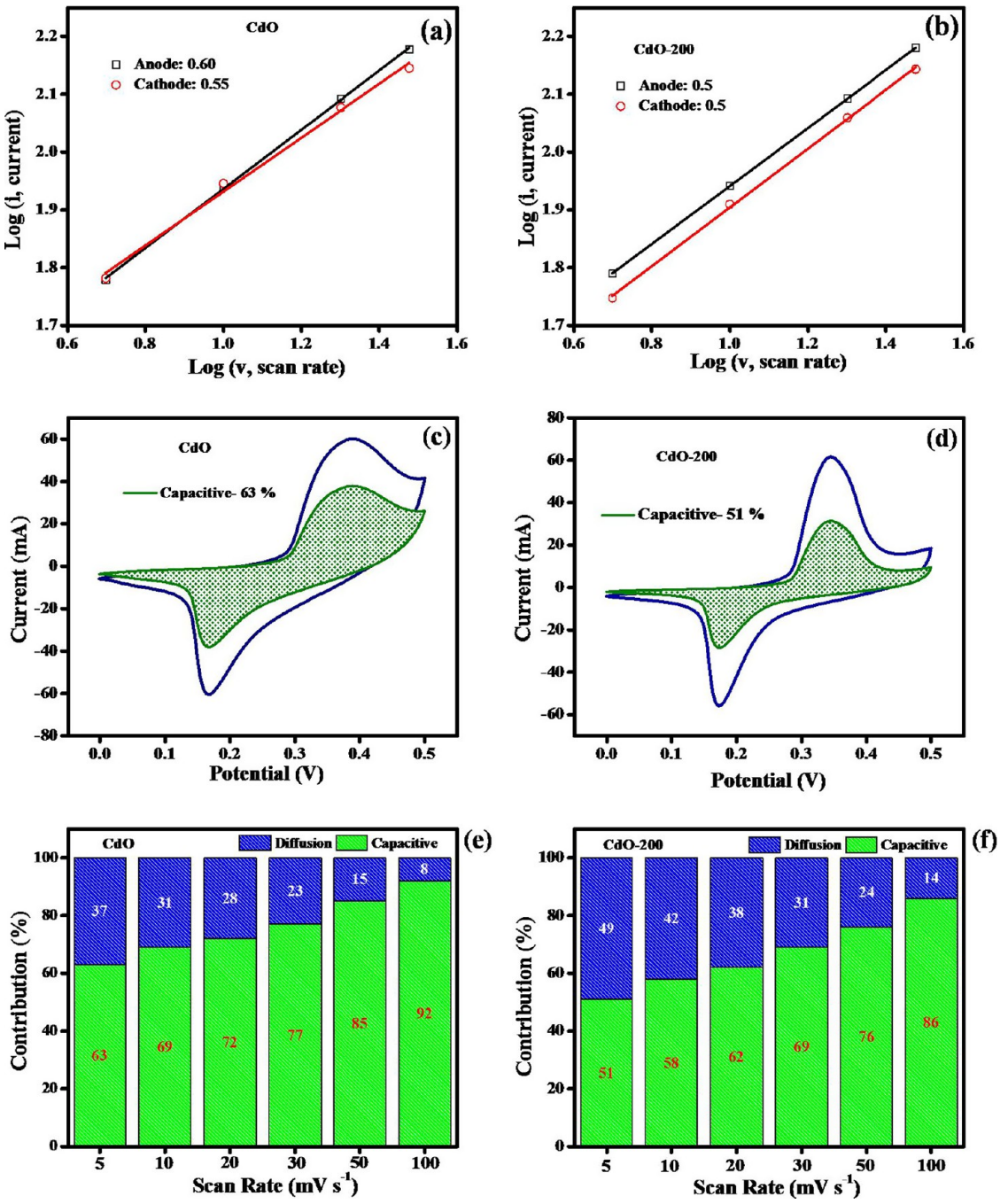

Figure 8. Calculated b-values of (a) CdO and (b) CdO-200, Capacitive-Diffusive contribution of (c) CdO and (d) CdO-200 at 5 mV s^{-1}, and Capacitive-Diffusive contribution of (e) CdO and (f) CdO-200 at different scan rates.

energy region such that the main peaks of Cd $3d_{3/2}$ and Cd $3d_{5/2}$ orbitals are located at 405.18 and 411.87 eV, respectively. The binding energy difference between the doublet peaks of Cd $3d_{3/2}$ and Cd $3d_{5/2}$ is found to be 6.69 eV. Interestingly, at the 200 shock conditions, the generation of two new additional peaks is witnessed at the higher energy region. Notably, the Cd $3d_{3/2}$ region has two peaks at 405.05 and 407.39 eV while the Cd $3d_{5/2}$ region has two peaks at 411.89 and 413.13 eV. Under the 200-shocked condition, the binding energy difference between the doublet peaks of Cd $3d_{3/2}$ and Cd $3d_{5/2}$ is found to be 6.84 eV (Figure 6d) and this higher value is probably due to the morphological changes from rod to honeycomb structures.

The linear enhancement of the binding energy difference between the doublet peaks with respect to the number of shock pulses occurs because of the lattice compression effect. The generation of a couple of tiny peaks in the higher energy region may be due to the formation of the secondary phase of B2 under the 200 shock conditions such that the observations are found to be well-matched with the XRD results. Similarly, O 1s spectra also show considerable changes with respect to the number of shock pulses (Figure 6e–g). Significantly, the control and 100-shocked CdO samples' O1 s spectra do not show significant differences in the shapes of the peaks; however, the peaks have undergone slight peak shift changes. Impressively, at the 200-shocked condition, there is a clear

https://doi.org/10.1021/acs.inorgchem.3c03461
Inorg. Chem. 2024, 63, 576−592

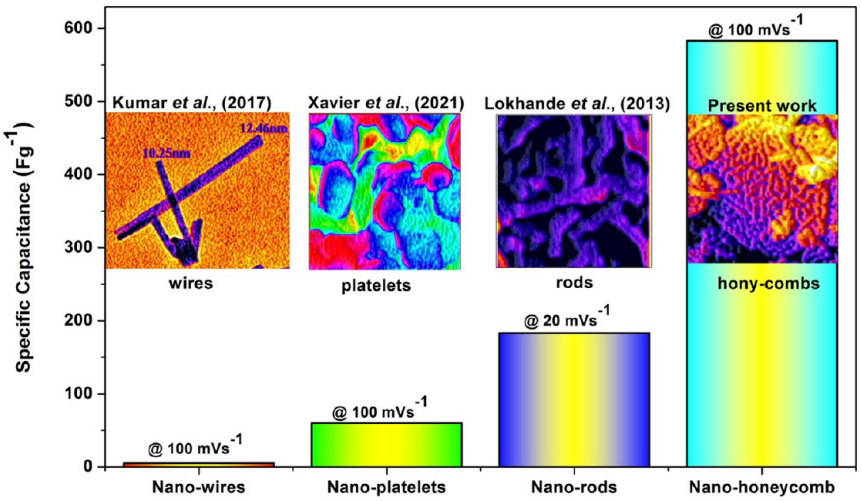

Figure 9. Comparison morphological feature-dependent specific capacitance of the CdO nanostructures.

indication for the formation of a new peak at 534 eV which may be the authentication of the formation B2 phase.

3.5. Electrochemical Analysis. The electrochemical property such as specific capacitance is highly sensitive to the crystallographically driven structural phase transitions as well as size and shape modifications of the test samples with the same mother phase.[29,33−35] Due to the outstanding shape modifications and presence of the secondary phase under shocked conditions, it is suspected that the electrochemical properties of the CdO NPs could experience a lot of changes so that the electrochemical analysis of the control and shocked CdO NPs has been performed and the recorded CV loops are presented in Figure 7. From the obtained CV loops (Figure 7a−c) the control and shocked CdO NPs samples represent strong redox peaks which clearly demonstrate the universal capacitive behavior as the CV loops are highly governed by faradaic reactions.[68] As shown in (Figure 7a−c), the shape of the CV curves and redox peaks represent the pseudotype behavior of the material which stores charges through surface/near surface redox reactions at the electrode and electrolyte interface.[70] The well-defined redox pairs describe the surface redox reactions of CdO wherein the redox transitions of Cd^{2+}/Cd^{3+} states follow the eqs 1 and 2. At the scan rate of 5 mV s^{-1}, the oxidation peak of CdO NPs nearly at 0.34 V represents the Cd^{2+}/Cd^{3+} transition and the reduction peak at about 0.17 V represents the Cd^{3+}/Cd^{2+} transition as well.[71]

$$CdO + H_2O + OH^- + e^- \leftrightarrow Cd(OH)_3^- \quad (1)$$

$$Cd(OH)_3^- + OH^- + e^- \leftrightarrow Cd(OH)_4^{2-} \quad (2)$$

Using the area enclosed in the CV, the corresponding specific capacitance (F g^{-1}) of the prepared samples' electrodes was calculated using the equation,

$$C = \frac{\int I dv}{2m \times \Delta V \times v} \quad (3)$$

where $\int Idv$ represents the integral area of the CV, m is the active mass of the electrode material, Δv is the scanned potential window (mV s^{-1}), and v is the scan rate. From the scan rate-dependent CV loops along different potential ranges as in Figure 7d, the control and shocked CV loops are presented at 100 mV s^{-1} and based on the obtained results, it is clear that the CV loop area has sufficiently increased at the 200 shock condition, which may be due to the dominant features of the honeycomb surface morphology of the CdO NPs.

The control of the CdO NPs' specific capacitance is mostly governed by the rod-shaped particles. The specific capacitances of the control and shocked samples have been calculated using the standard electrochemical relations and the obtained scan rate-dependent specific capacitance profiles are presented in Figure 7e. Furthermore, the specific capacitance of the samples at 100 mV s^{-1} with respect to the number of shock pulses is shown in Figure 7f. The CV current response of a material can be contributed by two factors that are capacitive current contribution and a slow diffusion-controlled process. The slow diffusion-controlled process can be distinguished from the capacitive contribution by using the power law.[72]

$$i = av^b \quad (4)$$

In eq 4, v is a CV scan rate, i corresponds to peak current, a and b are constants, and the b-value is constrained to fall in the range of 0.5−1. If b equals 1, the system will be capacitive. If b = 0.5, the system will be diffusive. The b-values for CdO and CdO-200 are obtained by taking the log of anodic peak currents versus the log of their corresponding scan rates. The b-values of CdO material are 0.6 for anodic and 0.55 for cathodic peak current responses, representing the charge storage mechanism which is mainly dominated by a slow-diffusion-controlled process (Figure 8a). The obtained b-value of CdO-200 for both anodic and cathodic peak currents is 0.5 (Figure 8b) which indicates the charge storage mechanism that is robustly dominated by the diffusive process compared to CdO. Furthermore, the contributions of the capacitive and slow-diffusive controlled mechanism are calculated quantitatively by the Dunn method using the following equation.[73]

$$i = k_1 v + k_2 v^{1/2} \quad (5)$$

Here k_1 and k_2 are constants that can be evaluated from the slope and intercept of a linear plot of $i(V)/v^{1/2}$ versus $v^{1/2}$, respectively, and v is the scan rate. The CV current response at 5 mV s^{-1} of the material CdO is calculated (Figure 8c), which shows the capacitive mechanism dominating the overall current response (63% capacitive behavior).

Even though the current response is dominated mostly by capacitive behavior, the peak current responses are mostly dominated by diffusive behavior resulting in b-values equal to

https://doi.org/10.1021/acs.inorgchem.3c03461
Inorg. Chem. 2024, 63, 576−592

0.5. This is also evident such that the CV response of CdO-200 is almost equally (51%) governed by the capacitive behavior at 5 mV s^{-1} (Figure 8d). From these findings, it is apparent that the material stores charge more strongly through the diffusive process after the shock treatment than before the shock treatment. The capacitive-diffusive contributions of CdO and CdO-200 are calculated and shown in Figure 8e,f. It is evident that, on increasing the scan rate, the diffusive mechanism decreases because of the fast movements of charges across the material thereby decreasing the time for the ions to diffuse into the lattices of active materials. So, the capacitive process mainly dominates the contribution to the overall CV current response.

According to the obtained profiles of specific capacitance, the values of the control, 100, and 200-shocked CdO NPs are found to be 433, 415, and 583 F g^{-1}, respectively at 100 m V s^{-1}. In a previous report, Kumar et al.[50], have reported the specific capacitance of the rod-shaped CdO NPs such that the obtained value is 183 F g^{-1} at 20 m V s^{-1} while for the CdO nanowires[56] and nanoplatelets,[57] the reported values of specific capacitance are 5 and 60 at 100 mV s^{-1}, respectively, and the corresponding profile is showcased in Figure 9. The materials of the honeycomb structure have attracted a lot of interest among the prominent candidates because of their high surface area, big voids to buffer volume changes, effective electron transfer, and excellent reaction kinetics for lithium transport, all of which lead to improved efficiency. From crashworthiness aspects, the honeycomb structure is particularly a good choice as an energy absorber, as well as for energy storage processes. In a honeycomb structure, the honeycomb cellular arrangement comprises evenly distributed double-layered hexagonal cells as derived from a natural honeycomb in a nest which enhances the energy-absorbing capacity of individual cells that is inclined with improved capacity compared to other morphological patterns.[74]

In this perspective, the obtained honeycomb structure possesses a unique three-dimensionally hierarchical porous structure with interconnected meso/macropore and abundant micropore, which can promote the mass transfer/diffusion of ions into the pores effectively, which offers a good environment for charge accumulation to give rise to excellent performance as an electrode material for supercapacitors. Furthermore, the honeycomb-like structure's large pores can tolerate volume expansion while still increasing the region between the active materials and the electrolyte. These outcomes further demonstrate that honeycomb-CdO nanostructures possess high capacitance, excellent rate performance, and cycle stability compared to the other morphological patterns. Based on the obtained results, it is clear that the surface morphology of the test sample has played an imperative role in the ability of energy storage, and the obtained higher efficiency of the 200-shocked CdO NPs is because of the formation of honeycomb surface morphology, which provides higher active sites in the surface due to the high surface area than that of rod-shaped particles. Note that the honeycomb structures are made up of very shot rods with hexagonal patterns and these advanced morphological features are beneficial for excellent supercapacitors to yield higher performance.[75−78]

The specimens are cycled for 5000 CV cycles at 100 mV s^{-1} to evaluate the stability for a long run (Figure 10). The capacitive retention of the materials CdO, CdO-100, and CdO-200 are 91.3, 93.7, and 95.4%, respectively. The materials exhibit a better cyclability even after 5000 CV cycles which

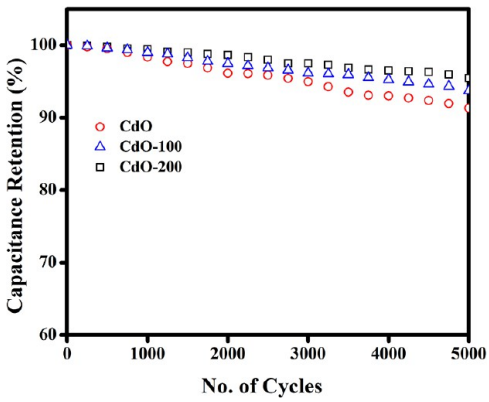

Figure 10. Cycle stability of materials CdO, CdO-100, and CdO-200.

shows the materials involve complete reversible reactions and minimum material degradations even after a long run. The materials are also characterized by XRD and XPS after 5000 cycles to analyze the phase and composition of the materials. From Figures S1 and S2, the XRD shows no phase change and no appearance of additional peaks in the materials after 5000 cycles which confirms that the charge storage mechanism involved a complete reversible reaction on the surface/near surface of the materials. However, from the XRD and XPS analyses, a slight difference could be observed in the intensity and full width at half-maximum aspects which may be because of the addition of binding polymer (PVDF) and conductive carbon black.

The practical suitability of CdO and CdO-200 was evaluated by constructing an asymmetric supercapacitor (ASC). The ASC was assembled by using CdO as the positive electrode and activated charcoal (AC) as the negative electrode. The electrochemical properties of AC have been evaluated by CV measurements within the operating potential window of −1 to 0 V (vs Ag/AgCl) at various scan rates in 3 M KOH electrolyte (Figure 11a). The CV spectrum of AC is almost rectangular, suggesting that charge storage mainly depends on the formation of the electric double layer. The capacitance of the AC is also calculated at different scan rates using CV. The calculated capacitances are 638, 514, 463, 400, 310, and 219 F g^{-1} at 5, 10, 20, 40, 60, 80, and 100 mV s^{-1}(Figure 11b).

From Figure 11c extrema of the CV sweeps of CdO-200 and AC, the operating potential range for an asymmetric device (ASC) is determined to be 1.5 V. The ASC single-cell device was constructed using 3 M KOH as an aqueous electrolyte. For the comparative analysis, the ASCs have been constructed using both CdO and CdO-200 (denoted as CdO//AC, and CdO-200//AC) to analyze the electrochemical behavior of the control and 200 shocked CdO samples. The CV curves of ASCs (Figure 11d,e) show distinct redox peaks, which indicate that the charge storage mechanism is mainly dominated by the redox mechanism, suggesting that the CdO electrode material mainly contributes to the charge storage process. Compared to CdO//AC, the CdO-200//AC exhibits a better current response, representing better electrochemical performance. The specific capacitances of the devices are calculated from CV curves and plotted against their corresponding scan rates (Figure 11f). The specific capacitance of CdO-200//AC is 138 F g^{-1} at 10 mV s^{-1} which is 1.3 times higher than that of CdO//AC (105 F g^{-1} at 10 mV s^{-1}). Due to the higher specific capacitance, the honeycomb morphological CdO NPs

https://doi.org/10.1021/acs.inorgchem.3c03461
Inorg. Chem. 2024, 63, 576−592

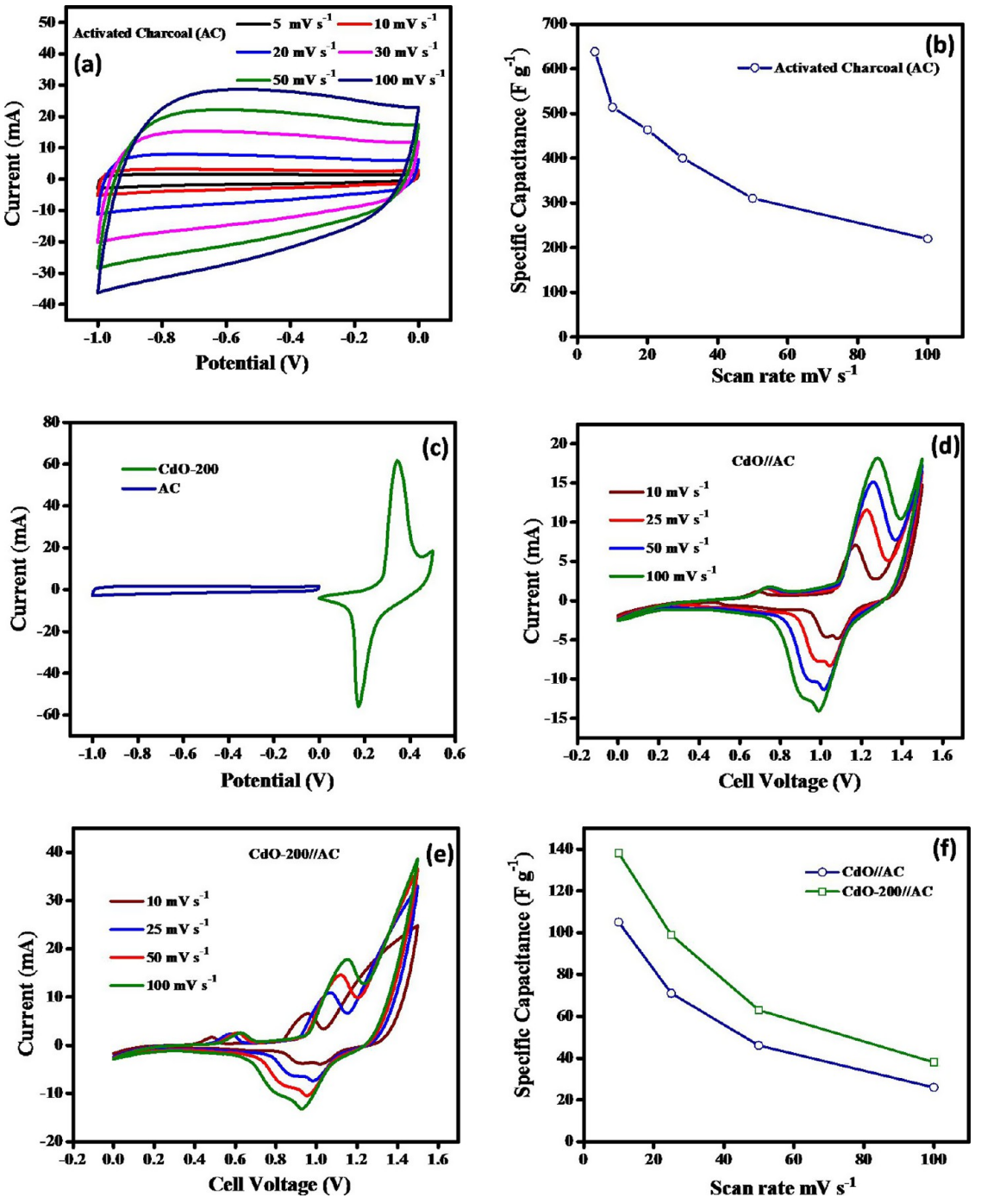

Figure 11. (a) CV curves of Activated Charcoal (AC), (b) specific capacitance vs scan rate plot of activated charcoal, (c) CV profiles of CdO-200 and activated charcoal, (d) CV spectrum of CdO//AC asymmetric supercapacitor (ASC) device, (e) CV curves of CdO-200//AC ASC device, and (f) specific capacitance vs scan rate plot of CdO//AC and CdO-200//AC devices.

are strongly suggested for practical energy storage device applications.[79−85]

3.8. BET Analysis. The Quanta Chrome Nova-1000 Brunauer−Emmett−Teller (BET) surface area analyzer was employed to assess the surface area and porosity of the control and 100 and 200 shocked CdO NPs through N2 adsorption−desorption measurements. The resulting isotherms exhibit characteristic IV-type behavior, indicating the mesoporous nature, as depicted in Figure 12. The BET surface area values for the control and 100 and 200 shocked CdO NPs are 16.268, 16.464, and 17.432 m^2 g^{-1}, respectively. Likewise, the corresponding pore volumes are 0.047, 0.027, and 0.022 cm^3 g^{-1}, while the pore diameters are 2.789, 2.187, and 1.96 nm, respectively. The observed results suggest that by subjecting the titled material to the chosen shock pulses, changes could be witnessed in its surface area, pore volume, and pore diameter. An increase in the surface area was obtained, whereas the decrease in pore diameters might have contributed to the enhanced specific capacitance of CdO at the 200-shocked condition.

3.9. Impedance Spectral Analysis. The electrochemical spectral analysis is provided for the procurement of impedance

https://doi.org/10.1021/acs.inorgchem.3c03461
Inorg. Chem. 2024, 63, 576−592

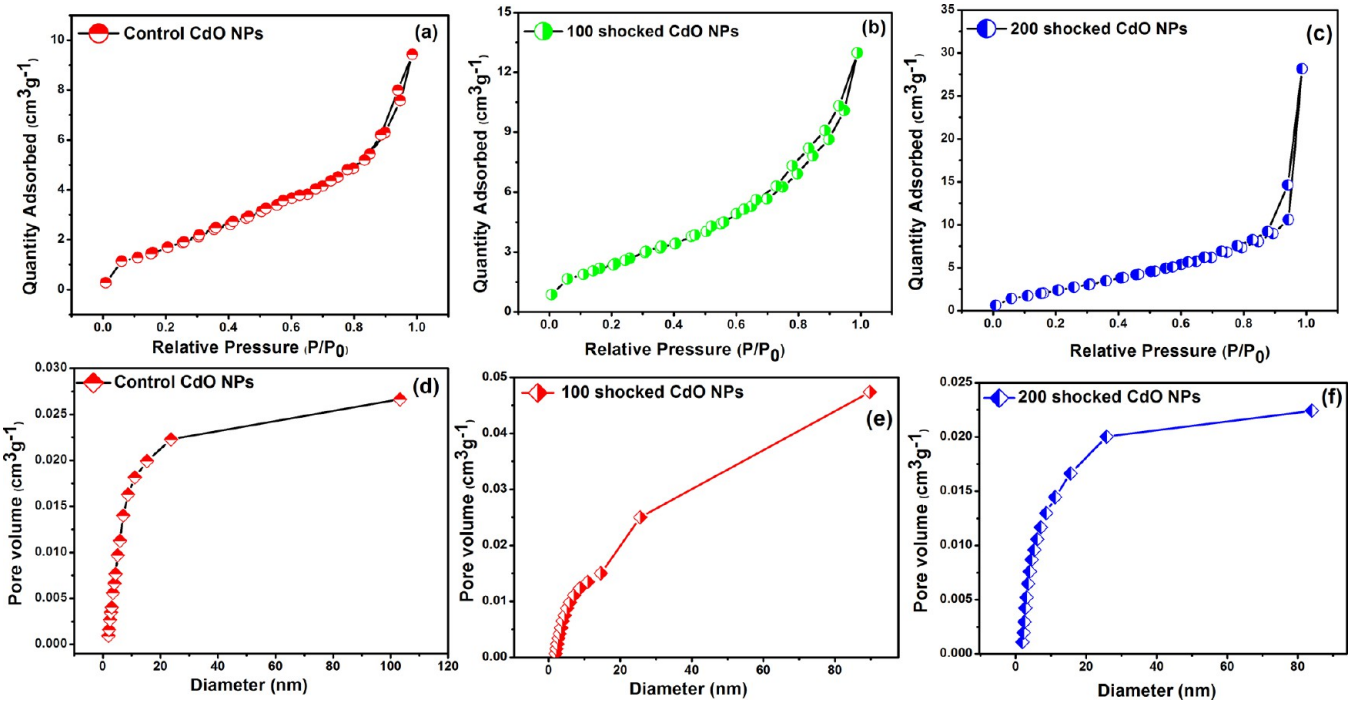

Figure 12. (a–c) N_2 adsorption desorption isotherm and (d–f) Pore size distribution of the control and shocked CdO samples.

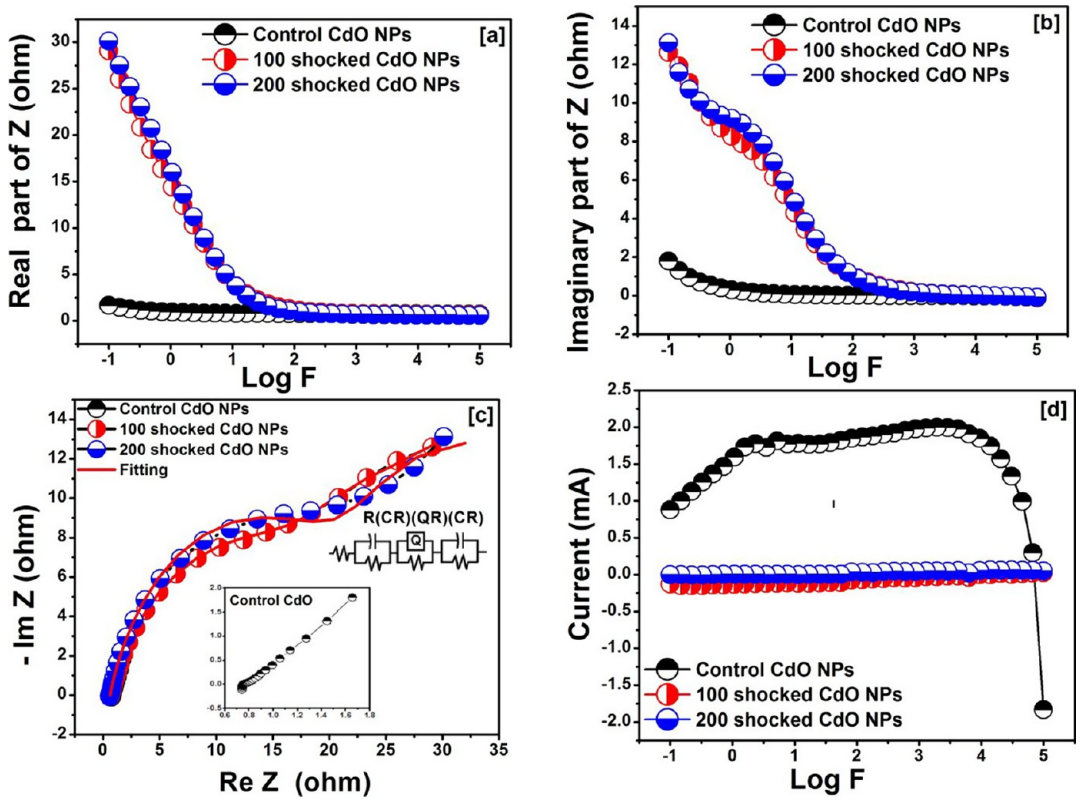

Figure 13. (a) Real part of the impedance (b) imaginary part of the impedance, (c) Cole–Cole plot, and (d) values of current for the control and shocked CdO NPs against the frequency.

spectral properties such as real and imaginary parts of impedance, Cole–Cole plot, and current profiles for the control and shocked CdO samples against the function frequency such that the obtained profiles are portrayed in Figure 13. As seen in Figure 13a,b, in the real and imaginary parts of the impedance profiles, the impedance values are high in the low-frequency region, and while increasing the applied frequency, the values of impedance are linearly reduced. Under shocked conditions, the real and imaginary parts of the impedance values are found to be increasing at lower frequency regimes which clearly illustrates that the total resistance behavior of the CdO NPs has significantly increased.

https://doi.org/10.1021/acs.inorgchem.3c03461
Inorg. Chem. 2024, 63, 576–592

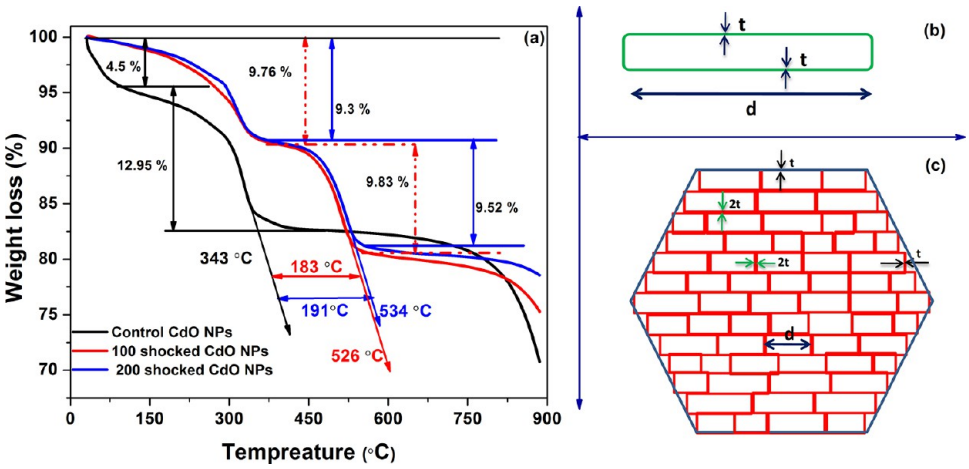

Figure 14. (a) TGA profiles of the control and shocked CdO NPs (b) typical diagram of the rod shape and (c) typical diagram of the honeycomb cell nanostructure CdO.

Moreover, the observed values of impedance at the 200-shocked condition are quite higher than that of the 100-shocked condition wherein the observed changes are probably due to the surface morphological changes and the presence of the secondary phase of B2 at the 200-shocked condition. As reflected in the FE-SEM images, the control sample has a lot of rod-shaped particles with a one-dimensional state and hence the electrons can have effective electronic transport ability between Cd and O without any electron collision because of the unavailability of the defects and grain boundaries as well as surface domain walls. Note that, at the 100-shocked condition, the rod-shaped particle density is considerably reduced whereas, at the 200-shocked condition, the rod-shaped particles almost disappear in such a way that the formation of hexagonal-shaped honeycomb nanostructures is witnessed.

The newly formed honeycomb nanostructures are much more complex compared to the simple one-dimensional nanorods, and the grain boundary density as well as the domain wall density inside the honeycomb nanostructure is significantly higher at the 200-shocked condition. Because of the abovementioned reasons, there could be a rapid decrease in the percolation threshold of the electrons in the crystal lattice so that the net electrical conductivity of the CdO NPs is significantly reduced. To verify this physical interpretation of the electrical conductivity behavior, the Cole−Cole plot and current profiles of the control and shocked CdO NPs are provided in Figure 13c,d. As seen in the control CdO NPs, the Cole−Cole plot has an incomplete semicircle and the width of the arc is low, whereas, at 100 and 200-shocked conditions, the width of the incomplete semicircular arcs has significantly increased which clearly represents that the electrical conductivity of the shocked samples is low compared to the control sample. Notably, the electrical conductivity of a material is an intrinsic bulk property that, together with the spatial dimensions and shape of a sample of the material, determines the electrical conductivity of that sample. This theory is based on the intrinsic relation between activation energy and surface relaxation factors. As per the observed morphological features, the control sample has rod-shaped particles and the 200-shocked CdO sample has honeycomb shapes. The length of the rod-shaped particles is considerably low compared to the honeycomb structures, whereas the diameter of the rod-shaped particles is significantly higher than that of the honeycomb structures. In total, the area of the rod-shaped particles is much lower than that of the honeycomb structures, and hence, the number of surface atoms is significantly higher than that of the honeycomb structures. As the volume of the nanosolid is the same as the volume of the nanosolid, the total number of atoms of the nanoparticle is the ratio of the particle volume to the atomic volume. By the quantum confinement theory, the holes in the valence band and the electrons in the conduction band are confined by the potential barriers of the surface or the potential well of the quantum box. The potential barrier is much lower in the rod-shaped particles compared to the honeycomb structures due to the significantly smaller size particles. In addition, rod-shaped nanostructures have a defect-free surface which leads to less electron collision and low activation energy compared to the honeycomb nanostructures. Therefore, the rod-shaped particles have higher electronic conductivity compared to the honeycomb nanostructures. As the outcomes of the optical properties (Figures S3 and S4) and magnetic properties (Figure S5) are well-aligned with the observations made on the structural and morphological features of the control and shocked samples, a detailed discussion of the abovementioned plots is provided in the Supplementary Section.

3.10. Thermogravimetric Analysis. It is generally considered that the honeycomb model structures possess superior thermal and mechanical stability compared to one-dimensional nanostructures[86,87] such that the thermal stability of the rod-shaped as well as honeycomb cell structures of CdO is analyzed and the obtained TGA plots are presented in Figure 14a while the DSC plots are displayed in Figure S6. As seen in Figure 14a, the control and shocked CdO samples undergo mass loss with two stages over the temperature region from 35 to 890 °C. During the first stage, the weight loss percentage is 4.5, 9.76, and 9.3% for the 0, 100, and 200 shocked conditions, respectively. The second stage weight loss profile is very crucial as the role of the rod-shaped and honeycomb nanostructures can be clearly extracted. The control CdO NRs show the end point of the second stage weight loss of 12.95% at 343 °C which is well-matched with the previously reported CdO NPs.[88−90] Interestingly, a significant change could be seen in the end point of the second stage inorganic matrix weight loss of the shocked CdO NPs such that the end points of the 100-shocked and 200-shocked conditions are 526 and 534 °C,

https://doi.org/10.1021/acs.inorgchem.3c03461
Inorg. Chem. 2024, 63, 576−592

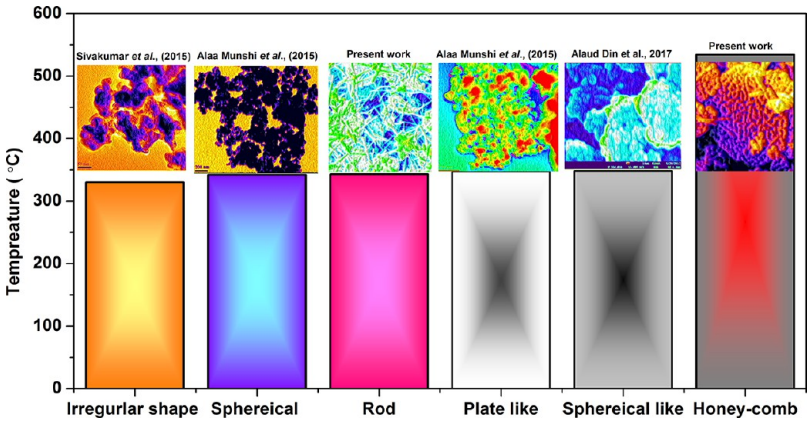

Figure 15. Comparison of second stage inorganic matrix weight loss end point temperature values of different morphological features of CdO.

respectively. Based on the obtained TGA profiles, the positive shift of the second stage end temperature point is because of the formation of honeycomb nanostructures at the 200-shocked condition, and the possible reasons for this large shift in decomposition temperature point are, as seen in FE-SEM images, that at the 200-shocked condition, the honeycomb nanostructures are made up of ultrasmall nanotubular grains such that the thickness of walls inside the honeycomb cell must be higher than the rod-shaped CdO and the typical schematic diagrams are presented in Figure 14b,c.

As seen in Figure 14b, the rod-shaped structure's wall thickness is considered as *t*, which is almost equal to both sides of the length aspects. However, the honeycomb nanostructures of CdO have a large number of 2*t* thickness walls inside the honeycomb wherein the sizes of the grains (d) are ultrasmall than the CdO nanorods. In addition to the above-mentioned factors, the two tubular grains parallel to each other provide flexural stiffness, while the structure supports the entire panel against the stress (mechanical and thermal) placed on it. Due to this reason, higher thermal energy is required to decompose the actual structural matrix of the honeycomb. It is evident that the observed stabilization of the nanostructure and decrease in grain growth can be obtained by reducing either mobility (the so-called kinetic approach) or the driving force (the so-called thermodynamic approach)[91,92] which is well-matched with the equivalent damper model of honeycomb structures.[92] Based on the abovementioned morphological patterns reasons, the honeycomb nanostructures have higher thermal stability than that of the rod-shaped CdO. As per the previous reports, the honeycomb nanostructures have much higher thermal stability than that of the conventional nanostructures (Figure 15).[88−90]

3.11. Implications of the Effect of Shock Waves on the Functional Properties of CdO. The shock wave is a type of mechanical wave that possesses a high pressure and high temperature within a narrow nanometer region. Shock waves can provide real-time impact problems such as dynamic impact, high stress, high pressure, high temperature, large mechanical force, etc. Moreover, until this point in time, only limited scientific knowledge is well-established on the shock wave impacts on solid-state materials such that it must be enhanced to understand the actual outcome of the shock wave impacts on solids in such a way that it would provide a potential chance to understand better the usual and unusual behavior of materials against the temperature and pressure. When such kind of acoustical shock waves are exposed to the solid-state samples, they can propagate within the solids and make them recrystallize within milliseconds because of the impact of the high temperature and high pressure. Generally, such shock waves induce rapid crystallization (dynamic recrystallization) within a few milliseconds. The degree of recrystallization and shock wave-induced premelting by superheating processes highly depend on the nature of materials and their thermal transport properties such as thermal diffusivity and thermal conductivity. During the shocked conditions, many plastic deformations and recrystallization processes can take place which leads to a lot of structural transitions and property changes. The changes in properties highly depend on structural transitions such as the ordered state to disordered state or disordered state to ordered state, shape changes, and deformation levels. For instance, Koteeswara Reddy et al. found the enhancement of electrical resistance from 11 to 50 Ω cm^{-2} due to the enhancement of the sp^3 carbons in the graphitic carbon nanoparticles under shocked conditions.[93] The optical transmittance rapidly increased from 37 to 64% at 800 nm during the transition of the glassy state to the crystalline state of Li_2SO_4 under shocked conditions due to the reduction of the positional disorder of Li^{2+} ions.[94] The saturation magnetization of the reduced graphene oxide is found to have reduced to 0.8633, 0.414, 0.2196, and 0.178 emu g^{-1} with respect to the number of shock pulses 0, 100, 200, and 400, respectively, because of the linear enhancement of the sp^2 hybridization carbon. The enhancement of graphitization takes place due to the shock wave-induced hot-spot nucleation process.[59] Thermal diffusivity is found to be enhanced from 0.678 to 1.552 × 10^{-6} m^2 s^{-1} because of the enhancement of the degree of crystalline nature in the ammonium dihydrogen phosphate (ADP) crystal.[60] Based on these findings, it is asserted that shock waves can effectively change the functional properties such as electrical, optical, thermal, and magnetic properties such that the change in magnitude is highly dependent on the types of structural transitions. In the present study, under the shocked conditions, the electrical conductivity and optical transmittance are found to be reduced with respect to the number of shock pulses, whereas the specific heat capacitance and melting points are found to be increased with respect to the number of shock pulses.

4. CONCLUSIONS

The shock wave processing on CdO NRs and the experimental results on their structural, morphological, and functional properties have been successfully demonstrated. Based on

https://doi.org/10.1021/acs.inorgchem.3c03461
Inorg. Chem. 2024, 63, 576−592

the obtained XRD, and HR-TEM results, it is authenticated that, under shocked conditions, the CdO undergoes slight lattice compression which results in the formation of the B2 phase as the secondary phase under the 200-shocked condition. The FE-SEM analysis provides convincing results in such a way that the rod-shaped structures are converted into honeycomb-like structures due to the dynamic recrystallization and solid-state fusion processes and such a type of nanostructure is not reported, to date, for the title material. The cyclic voltammetric analysis clearly represents the values of current density and specific capacitance which are higher for the 200-shocked CdO NPs (honeycomb structure) compared to the control and 100-shocked samples because of the presence of higher-density active sites on the surface of the particles and the calculated values of specific capacitance are 433, 415, and 583 F g^{-1}, respectively, for the 0, 100, and 200-shocked samples at the scan rate 100 mV s^{-1}. The electrical conductivity behavior is considerably reduced while increasing the number of shock pulses which is due to the shape conversion of the particles from the nanorods to the nano honeycombs. TGA results show outstanding thermal stability of the honeycomb nanostructures compared to that of the rod-shaped CdO particles as well as other forms of nanostructures such as nanoplates and nanospheres. The functional properties such as optical transmittance and saturation magnetization show subtle changes that are based on the lattice compression and the effects of morphological change; thereby, the formation of the B2 phase is witnessed at the 200-shocked condition. Based on the outcomes of the present experimental data, the proposed method can be listed as a prominent postprocessing extreme environmental condition technique for the nanoparticles which include the diamond anvil cell, laser shock waves, and high energy particle irradiation. Furthermore, the present experimental results reveal that the value of specific capacitance has increased for the shock wave-induced honeycomb structures; thereby, they are very much suitable for energy storage device applications.

■ ASSOCIATED CONTENT

Supporting Information

The Supporting Information is available free of charge at https://pubs.acs.org/doi/10.1021/acs.inorgchem.3c03461.

Additional experimental details of the shock wave loading procedure; optical and magnetic properties for the control and shocked samples (PDF)

■ AUTHOR INFORMATION

Corresponding Author

Lidong Dai − *Key Laboratory of High-Temperature and High-Pressure Study of the Earth's Interior, Institute of Geochemistry, Chinese Academy of Sciences, Guiyang, Guizhou 550081, China;* orcid.org/0000-0002-9081-765X; Email: dailidong@vip.gyig.ac.cn

Authors

Sivakumar Aswathappa − *Key Laboratory of High-Temperature and High-Pressure Study of the Earth's Interior, Institute of Geochemistry, Chinese Academy of Sciences, Guiyang, Guizhou 550081, China*

S. Sahaya Jude Dhas − *Department of Physics, Kings Engineering College, Chennai, Tamilnadu 602117, India*

S. A. Martin Britto Dhas − *Shock Wave Research Laboratory, Department of Physics, Abdul Kalam Research Center, Sacred Heart College, Tirupattur, Tamil Nadu 635601, India;* orcid.org/0000-0003-0896-7534

Sourav Laha − *Department of Chemistry, National Institute of Technology Durgapur, Durgapur 713209, India*

Raju Suresh Kumar − *Department of Chemistry, College of Science, King Saud University, Riyadh 11451, Saudi Arabia;* orcid.org/0000-0003-3754-4223

Abdulrahman I. Almansour − *Department of Chemistry, College of Science, King Saud University, Riyadh 11451, Saudi Arabia*

Complete contact information is available at: https://pubs.acs.org/10.1021/acs.inorgchem.3c03461

Author Contributions

L.D. conceived the idea and led the project. S.A. performed the acoustic shock wave measurements. L.D., S.A., S.S.J.D., S.A.M.B.D., S.L., R.S.K., and A.I.A. contributed to the analysis, interpretation, and discussion of results. A.S. wrote the manuscript with the help of all the authors. All the authors commented on the final manuscript. L.D. supervised the project.

Notes

The authors declare no competing financial interest.

■ ACKNOWLEDGMENTS

The authors thank to NSF of China (42072055). The project was supported by Researchers Supporting Project number (RSP2023R231), King Saud University, Riyadh, Saudi Arabia.

■ REFERENCES

(1) Chen, Y.; Lai, Z. C.; Zhang, X.; Fan, Z. X.; He, Q. Y.; Tan, C. L.; Zhang, H. Phase engineering of nanomaterials. *Nat. Rev. Chem.* **2020**, *4*, 243−256.

(2) KrAsheninnikov, A. V.; Banhart, F. Engineering of nanostructured carbon materials with electron or ion beams. *Nat. Mater.* **2007**, *6*, 723−733.

(3) Oganov, A. R.; Pickard, C. J.; Qiang, Z.; Needs, R. J. Structure prediction drives materials discovery. *Nat. Rev. Mater.* **2019**, *4*, 331−348.

(4) Calum, K.; Moore, T. L.; Lorenzo, L. R.; Rutishauser, B. R.; Fink, A. P. Form follows function: Nanoparticle shape and its implications for nanomedicine. *Chem. Rev.* **2017**, *117*, 11476−11521.

(5) Zhang, H. Y.; Ji, Z. X.; Tian, X.; et al. Use of metal oxide nanoparticle band gap to develop a predictive paradigm for oxidative stress and acute pulmonary inflammation. *ACS Nano* **2012**, *6*, 4349−4368.

(6) Cao, S. W.; Tao, F.; Tang, Y.; Li, Y. T.; Yu, J. G. Size- and shape-dependent catalytic performances of oxidation and reduction reactions on nanocatalysts. *Chem. Soc. Rev.* **2016**, *45*, 4747−4765.

(7) Baig, N.; Kammakakam, I.; Wail, F. Nanomaterials: A review of synthesis methods, properties, recent progress, and challenges. *Mater. Adv.* **2021**, *2*, 1821.

(8) Gawande, M. B.; Goswami, A.; Felpin, F. X.; Asefa, T.; Huang, X. X.; Silva, R.; Zou, X. X.; Zboril, R.; Varma, R. S. Cu and Cu-Based nanoparticles: Synthesis and applications in catalysis. *Chem. Rev.* **2016**, *116*, 3722−3811.

(9) Bai, F.; Bian, K. F.; Huang, X.; Wang, Z. W.; Fan, H. Y. Pressure induced nanoparticle phase behavior, property, and applications. *Chem. Rev.* **2019**, *119*, 7673−7717.

(10) Horvath-Bordon, E.; Riedel, R.; Zerr, A.; McMillan, P. F.; Auffermann, G.; Prots, Y.; Bronger, W.; Kniep, R.; Kroll, P. High-pressure chemistry of nitride-based materials. *Chem. Soc. Rev.* **2006**, *35*, 987−1014.

(11) Su, Z.; Shaw, W. L.; Miao, Y. R.; You, S.; Dlott, D. D.; Suslick, K. S. Shock wave chemistry in a metal−organic framework. *J. Am. Chem. Soc.* **2017**, *139*, 4619−4622.
(12) Zhou, X.; Miao, Y. R.; Shaw, W. L.; Suslick, K. S.; Dlott, D. D. Shock wave energy absorption in metal−organic framework. *J. Am. Chem. Soc.* **2019**, *141*, 2220−2223.
(13) Flores-Rojas, G. G.; López-Saucedo, F.; Bucio, E. Gamma-irradiation applied in the synthesis of metallic and organic nanoparticles: A short review. *Radiat. Phys. Chem.* **2020**, *169*, 107962.
(14) Dehghani, Z.; Nezamdoost, S.; Vejdani Noghreiyan, A.; Nadafan, M. The influence of γ-irradiation on molecular structure and mass attenuation coefficients of γ-Al_2O_3 nanoparticles. *AIP Adv.* **2023**, *13*, No. 035120.
(15) Gómez-Navarro, C.; Pablo, P. D.; Gómez-Herrero, J.; Biel, B.; Garcia-Vidal, F. J.; Rubio, A.; Flores, F. Tuning the conductance of single-walled carbon nanotubes by ion irradiation in the Anderson localization regime. *Nat. Mater.* **2005**, *4*, 534−539.
(16) Banhart, F.; Li, J. X.; Krasheninnikov, A. V. Carbon nanotubes under electron irradiation: stability of the tubes and their action as pipes for atom transport. *Phys. Rev. B* **2005**, *71*, No. 241408, DOI: 10.1103/PhysRevB.71.241408.
(17) Vasu, K.; Matte, H. S. S. R.; Shirodkar, S. N.; Jayaram, V.; Reddy, K. P. J.; Waghmare, U. V.; Rao, C. N. R. Effect of high-temperature shock-wave compression on few-layer MoS_2, WS_2 and $MoSe_2$. *Chem. Phys. Lett.* **2013**, *582*, 105−109.
(18) Maity, T. K.; Gopinath, N. K.; Janardhanraj, S.; Biswas, K.; Basu, B. Computational and microstructural stability analysis of shock wave interaction with NbB_2B_4C based nanostructured ceramics. *ACS Appl. Mater. Interfaces.* **2019**, *11*, 47491−47500.
(19) Jayaram, V.; Gupta, A.; Reddy, K. P. J. Investigation of strong shock wave interactions with CeO_2 ceramic. *J. Adv. Ceram.* **2014**, *3*, 297−305.
(20) Sivakumar, A.; Rita, A.; Sahaya Jude Dhas, S.; Martin Britto Dhas, S. A. Tuning of surface plasmon resonance of silver nano particles by shock waves for plasmonic device applications. *Opt. Laser. Technol.* **2020**, *128*, No. 106235.
(21) Samannan, B.; Chen, Y. S.; Selvam, J.; Peter, P.; Lin, Y. L.; Thavasikani, J. Shock waves impulses assisted hydrothermal method of synthesizing of organic 12-B polyanions and its applications. *Appl. Sur. Sci. Adv.* **2023**, *13*, No. 100359.
(22) Roy, A.; Singh, S. V.; Ambresh, M.; et al. Shock processing of amorphous carbon nanodust. *Adv. Space. Res.* **2022**, *70*, 2571−2581.
(23) Kalaiarasi, S.; Sivakumar, A.; Martin Britto Dhas, S. A.; Jose, M. Shock wave induced anatase to rutile TiO_2 phase transition using pressure driven shock tube. *Mater. Lett.* **2018**, *219*, 72−75.
(24) Jayaram, V.; Reddy, K. P. J. Experimental study of the effect of strong shock heated test gases with cubic zirconia. *Adv. Mater. Lett.* **2016**, *8*, 100−150.
(25) Sivakumar, A.; Rita, A.; Sahaya Jude Dhas, S.; Reddy, K. P. J.; Kumar, R. S.; Almansour, A. I.; Chakraborty, S.; Moovendaran, K.; Sridhar, J.; Martin Britto Dhas, S. A. Dynamic shock wave driven simultaneous crystallographic and molecular switching between α-Fe_2O_3 and Fe_3O_4 nanoparticles−A new finding. *Dalton Trans.* **2022**, *51*, 9159−9166.
(26) Sivakumar, A.; Soundarya, S.; Jude Dhas, S. S.; Bharathi, K. K.; Dhas, S. M. Shock wave driven solid state phase transformation of Co_3O_4 to CoO nanoparticles. *J. Phys. Chem. C* **2020**, *124*, 10755−10763.
(27) Mowlika, V.; Sivakumar, A.; Martin Britto Dhas, S. A.; Naveen, C. S.; Phani, A. R.; Robert, R. Shock wave induced switchable magnetic phase transition behaviour of $ZnFe_2O_4$ ferrite nanoparticles. *J. Nanostruc. Chem.* **2020**, *10*, 203−209.
(28) Mowlika, V.; Naveen, C. S.; Phani, A. R.; Sivakumar, A.; Dhas, S. M.; Robert, R. Shock wave induced magnetic phase transition in cobalt ferrite nanoparticles. *Mater. Chem. Phys.* **2022**, *275*, No. 125300.
(29) Sivakumar, A.; Jude Dhas, S. S; Pazhanivel, T.; Almansour, A. I.; Kumar, R. S.; Arumugam, N.; Raj, C. J.; Dhas, S. M. Phase transformation of amorphous to crystalline of multiwall carbon nanotubes by shock waves. *Cryst. Growth. Des.* **2021**, *21*, 1617−1624.
(30) Jayaram, V.; Ranjith, R.; Bera, P. Non-catalytic behavior of SiO_2 fine powders in presence of strong shock waves for aerospace applications. *J. Mater. Sci. Appl.* **2018**, *4*, 37−46.
(31) Sivakumar, A.; Ramya, S.; Jude Dhas, S. S.; Almansour, A. I.; Kumar, R. S.; Arumugam, N.; Magesh, M.; Dhas, S. M. Assessment of crystallographic and electronic phase stability of shock wave loaded cubic cerium oxide nanoparticles. *Ceram. Int.* **2022**, *48*, 1963−1968.
(32) Rita, A.; Sivakumar, A.; Martin Britto Dhas, S. A. Influence of shock waves on structural and morphological properties of copper oxide NPs for aerospace applications. *J. Nanostruct. Chem.* **2019**, *9*, 225−230.
(33) Sivakumar, A.; Jude Dhas, S. S.; Almansour, A. I.; Kumar, R. S.; Arumugam, N.; Prabhu, S.; Sivashanmugan, K.; Ramesh, R.; Dhas, S. M. Shock waves induced enhancement of electrochemical properties of $CoFe_2O_4$ nanoparticles for energy storage applications. *Surf. Interfaces* **2021**, *27*, No. 101539.
(34) Sivakumar, A.; Jude Dhas, S. S.; Sivaprakash, P.; Dhayal Raj, A.; Kumar, R. S.; Arumugam, S.; Prabhu, S.; Ramesh, R.; Shubhadip, C.; Dhas, S. M. Shock wave recovery experiments on α-V_2O_5 nano-crystalline materials: A potential material for energy storage applications. *J. Alloys Compound.* **2022**, *929*, No. 167180.
(35) Sivakumar, A.; Mowlika, V.; Jude Dhas, S. S.; Prabhu, S.; Ramesh, R.; Robert, R.; Dhas, S. M. Shock wave induced switchable electrical resistance of $ZnFe_2O_4$ nanoparticles. *Solid State Sci.* **2022**, *125*, No. 106843.
(36) Piper, L. F. J.; De Masi, A.; Smith, K. E.; Schleife, A.; Fuchs, F.; Bechstedt, F.; Zuniga-Perez, J.; Munoz-Sanjose, V. Electronic structure of single-crystal rocksalt CdO studied by soft x-ray spectroscopies and ab initio calculations. *Phys. Rev. B* **2008**, *77*, No. 125204.
(37) Dakhel, A. A. Influence of dysprosium doping on the electrical and optical properties of CdO thin films. *Sol. Energy* **2009**, *83*, 934−939.
(38) Dakhel, A. A. Electrical and optical properties of iron-doped CdO. *Thin. Solid. Films* **2010**, *518*, 1712−1715.
(39) Henriquez, R.; Grez, P.; Munoz, E.; Dalchiele, E. A.; Marotti, R. E.; Gomez, H. Template-free non-aqueous electrochemical growth of CdO nanorods. *Thin Solid Films* **2011**, *520*, 41−46.
(40) Liu, H. Z.; Mao, H. K.; Somayazulu, M.; Ding, Y.; Meng, Y.; Häusermann, D. B1-to-B2 phase transition of transition-metal monoxide CdO under strong compression. *Phys. Rev. B* **2004**, *70*, No. 094114.
(41) Feng, P.; Chen, D.; Fu, H.; Cheng, X. Phase transition and elasticity of CdO under pressure. *Phys. Status Solidi B* **2009**, *246*, 71−76.
(42) King, P. D. C.; Veal, T. D.; Schleife, A.; Zúñiga-Perez, J.; Martel, B.; Jefferson, P. H.; Fuchs, F.; Muñoz-Sanjose, V.; Bechstedt, F.; McConville, C. F. Valence-band electronic structure of CdO, ZnO, and MgO from x-ray photoemission spectroscopy and quasi-particle-corrected density-functional theory calculations. *Phys. Rev. B* **2009**, *79*, No. 205205.
(43) Duan, Y.; Qin, L.; Tang, G.; Shi, L. First-principles study of ground- and metastable-state properties of XO (X = Be, Mg, Ca, Sr, Ba, Zn and Cd). *Eur. Phys. J. B* **2008**, *66*, 201−209.
(44) Guerrero-Moreno, R. J.; Takeuchi, N. First principles calculations of the ground-state properties and structural phase transformation in CdO. *Phys. Rev. B* **2002**, *66*, No. 205205.
(45) Feng, P.; Liu, Q.; Fu, H.; Yang, X. First-principles calculations on phase transition and elasticity of CdO under pressure. *Solid State Commun.* **2008**, *148*, 6−9.
(46) Piper, L. F. J.; Colakerol, L.; King, P. D. C.; et al. Observation of quantized sub-band states and evidence for surface electron accumulation in CdO from angle-resolved photoemission spectroscopy. *Phys. Rev. B* **2008**, *78*, No. 165127.
(47) Fan, D. H. Catalyst-free growth and crystal structures of CdO nanowires and nanotubes. *J. Cryst. Growth* **2009**, *311*, 2300−2304.

(48) Selvam, N. C. S.; Kumar, R. T.; Yogeenth, K.; John Kennedy, L.; Sekaran, G.; Vijaya, J. J. Simple and rapid synthesis of cadmium oxide (CdO) nanospheres by a microwave-assisted combustion method. *Powder Technol.* **2011**, *211*, 250−255.
(49) Munawar, T.; Nadeem, M. S.; Mukhtar, F.; Manzoor, S.; Ashiq, M. N.; Batool, S.; Hasan, M.; Faisal, I. Enhanced photocatalytic, antibacterial, and electrochemical properties of CdO-based nanostructures by transition metals co-doping. *Adv. Powder. Technol.* **2022**, *33*, No. 103451.
(50) Kumar, S.; Ahmed, B.; Ojha, A. K.; Das, J.; Kumar, A. Facile synthesis of CdO nanorods and exploiting its properties towards supercapacitor electrode materials and low power UV irradiation driven photocatalysis against methylene blue dye. *Mater. Res. Bull.* **2017**, *90*, 224−231.
(51) Ye, M.; Zhong, H.; Zheng, W.; Li, R.; Li, Y. Ultralong cadmium hydroxide nanowires: synthesis, characterization, and transformation into CdO nanostrands. *Langmuir* **2007**, *23*, 9064−9068.
(52) Guo, Z.; Li, M.; Liu, J. Highly porous CdO nanowires: Preparation based on hydroxy- and carbonate-containing cadmium compound precursor nanowires, gas sensing and optical properties. *Nanotechnology* **2008**, *19*, No. 245611.
(53) Gudla, U. R.; Suryanarayana, B.; Raghavendra, V.; Parajuli, D.; Murali, N.; Dominic, S.; Ramakrishna, Y.; Chandramouli, K. Structural, optical and luminescence properties of pure, Fe-doped and glucose-capped CdO Semiconductor nanoparticles for their antibacterial activity. *J. Mater. Sci: Mater. Electron.* **2021**, *32*, 3920−3928.
(54) Thambidurai, M.; Dang, C. Structural, morphological and optical properties of CdO nanostructures synthesized by chemical bath deposition method. *Mater. Lett.* **2018**, *221*, 244−247.
(55) Xia, W.; Liu, Y.; Li, J.; Chen, C. Investigation of CdO hexagonal nanoflakes synthesized by hydrothermal method for liquefied petroleum gas detection. *Anal. Methods* **2016**, *8*, 6265−6269.
(56) Lokhande, B. J.; Ambare, R. C.; Mane, R. S.; Bharadwaj, S. R. Boron-doped cadmium oxide composite structures and their electrochemical measurements. *Mater. Res. Bull.* **2013**, *48*, 2978−2983.
(57) Xavier, A. R.; Ravichandran, A. T.; Vijayakumar, S.; Angelin, M. D.; Rajkumar, S.; Merlin, J. P. Synthesis and characterization of Sr-doped CdO nanoplatelets for supercapacitor applications. *J. Mater. Sci: Mater. Electron.* **2022**, *33*, 8426−8434.
(58) Saha, M.; Ghosh, S.; De, S. K. Nanoscale kirkendall effect driven au decorated CdS/CdO colloidal nanocomposites for efficient hydrogen evolution, photocatalytic dye degradation and Cr (VI) reduction. *Catal. Today* **2020**, *340*, 253−267.
(59) Sivakumar, A.; Dai, L. D.; Jude Dhas, S. S.; Dhas, S. M.; Mowlika, V.; Kumar, R. S.; Almansour, A. I. Reduction of amorphous carbon clusters from the highly disordered and reduced graphene oxide NPs by acoustical shock waves−Towards the formation of highly ordered graphene. *Diam. Relat. Mater.* **2023**, *137*, No. 110139.
(60) Sivakumar, A.; Suresh, S.; Balachandar, S.; Thirupathy, J.; Kalyana Sundar, J.; Martin Britto Dhas, S. A. Effect of shock waves on thermophysical properties of ADP and KDP crystals. *Optic. Laser. Technol.* **2019**, *111*, 284−289.
(61) Lindsay, L.; Parker, D. S. Calculated transport properties of CdO: Thermal conductivity and thermoelectric power factor. *Phys. Rev. B* **2015**, *92*, No. 144301.
(62) Slack, G. A. Thermal conductivity of II-VI compounds and phonon scattering by Fe^{2+} impurities. *Phys. Rev. B* **1972**, *6*, 3761 DOI: 10.1103/PhysRevB.6.3791.
(63) Sivakumar, A.; Jude Dhas, S. S.; Almansour, A. I.; Kumar, R. S.; Arumugam, N.; Dhas, S. M. Spectroscopic assessment of shock wave resistance on ZnO nanorods for aerospace applications. *J. Inorg. Organomet. Polym. Mater.* **2021**, *31*, 2553−2559.
(64) Sivakumar, A.; Victor, C.; Muralidhr Nayak, M.; Dhas, S. M. Structural, optical, and morphological stability of ZnO nano rods under shock wave loading conditions. *Mater. Res. Express* **2019**, *6*, No. 045031.
(65) Wu, Y.; Frueh, J.; Si, T.; Möhwald, H.; He, Q. Laser-induced fast fusion of gold nanoparticles modified polyelectrolyte microcapsules. *Phys. Chem. Chem. Phys.* **2015**, *17*, 3281−3286.
(66) Turneaure, S. T.; Sharma, S. M.; Gupta, Y. M. Nanosecond melting and recrystallization in shock-compressed silicon. *Phys. Rev. Lett.* **2018**, *121*, No. 135701.
(67) Luo, S. N.; Ahrens, T. J. Shock-induced superheating and melting curves of geophysically important minerals. *Phys. Earth Planet. Inter.* **2004**, *143*, 369−386.
(68) Jeejamol, D. J.; Jai Aultrin, K. S.; Dev Anand, M. Exploration of CdO properties favoring superior photocatalytic degradation of methylene blue dye by Al^{3+} doping. *Opt. Quantum Electron.* **2022**, *54*, 291.
(69) Khallaf, H.; Chen, C. T.; Chang, L. B.; Lupan, O.; Dutta, A.; Heinrich, H.; Shenouda, A.; Chow, L. Investigation of chemical bath deposition of CdO thin films using three different complexing agents. *Appl. Surf. Sci.* **2011**, *257*, 9237−9242.
(70) Sarno, M. Nanotechnology in energy storage: the supercapacitors. *Stud. Surf. Sci. Catal.* **2020**, *179*, 431−458.
(71) Sajjad, M.; Shah, M. Z. U.; Mahmood, F.; Javed, M. F.; Maryam, R.; Ahmad, F.; Shah, A.; Hussain, R.; Toufiq, A. M.; Mao, Z.; Rahman, S. CdO nanocubes decorated on rGO sheets as novel high conductivity positive electrode material for hybrid supercapacitor. *J. Alloy. Compound.* **2023**, *938*, No. 168462.
(72) Augustyn, V.; Simon, P.; Dunn, B. Pseudocapacitive oxide materials for high-rate electrochemical energy storage. *Energy. Environ. Sci.* **2014**, *7*, 1597−1614.
(73) Simon, P.; Gogotsi, Y.; Dunn, B. Where do batteries end and supercapacitors begin? *Science* **2014**, *80*, 1210−1211.
(74) Sajjad, M.; Lu, W. Honeycomb-based heterostructures: An emerging platform for advanced energy applications: A review on energy systems. *Electrochem. Sci. Adv.* **2022**, *2*, No. e202100075.
(75) Chang, J.; Mane, R. S.; Ham, D.; Lee, W.; Cho, B. W.; Lee, J. K.; Han, S. H. Electrochemical capacitive properties of cadmium oxide films. *Electrochim. Acta* **2007**, *53*, 695−699.
(76) Wang, F.; Chen, L.; Li, H.; Duan, G.; He, S.; Zhang, L.; Zhang, G.; Zhou, G.; Jiang, S. N-doped honeycomb-like porous carbon towards high-performance supercapacitor. *Chin. Chem. Lett.* **2020**, *31*, 1986−1990.
(77) Han, Y.; Dong, X.; Zhang, C.; Liu, S. Easy synthesis of honeycomb hierarchical porous carbon and its capacitive performance. *J. Power. Sources* **2013**, *227*, 118−122.
(78) He, X.; Yu, H.; Fan, L.; Yu, M.; Zheng, M. Honeycomb-like porous carbons synthesized by a soft template strategy for supercapacitors. *Mater. Lett.* **2017**, *195*, 31−33.
(79) Wang, H.; Ren, X.; Chen, J.; Xu, W.; He, Q.; Wang, H.; Zhan, F.; Chen, L. Recent advances of emerging oxyhydroxide for electrochemical energy storage applications. *J. Power Sources* **2023**, *554*, No. 232309.
(80) Li, Y.; Huang, B.; Zhao, X.; Luo, Z.; Liang, S.; Qin, H.; Chen, L. Zeolitic imidazolate framework-L-assisted synthesis of inorganic and organic anion-intercalated hetero-trimetallic layered double hydroxide sheets as advanced electrode materials for aqueous asymmetric supercapacitor battery. *J. Power Sources* **2022**, *527*, No. 231149.
(81) Huang, B.; Wang, H.; Liang, S.; Qin, H.; Li, Y.; Luo, Z.; Zhao, C.; Xie, L.; Chen, L. Two-dimensional porous cobalt−nickel tungstate thin sheets for high performance supercapattery. *Energy Storage Mater.* **2020**, *32*, 105−114.
(82) Mao, L.; Zhao, X.; Li, Y.; Chen, L. New nickel-rich ternary carbonate hydroxide two-dimensional porous sheets for high-performance aqueous asymmetric supercapattery. *J. Colloid Interface Sci.* **2022**, *624*, 482−493.
(83) Wang, H.; He, Q.; Zhan, F.; Chen, L. Fe, Co-codoped layered double hydroxide nanosheet arrays derived from zeolitic imidazolate frameworks for high-performance aqueous hybrid supercapacitors and Zn-Ni batteries. *J. Colloid Interface Sci.* **2023**, *630*, 286−296.
(84) Li, Y.; Luo, Z.; Liang, S.; Qin, H.; Zhao, H.; Chen, L.; Wang, H.; Chen, S. Two-dimensional porous zinc cobalt sulfide nanosheet

https://doi.org/10.1021/acs.inorgchem.3c03461
Inorg. Chem. 2024, 63, 576−592

arrays with superior electrochemical performance for supercapatteries. *J. Mater. Sci. Technol.* **2021**, *89*, 199−208.
(85) Zhao, X.; Mao, L.; Cheng, Q.; Li, L.; Liao, F.; Yang, G.; Xie, L.; Zhao, C.; Chen, L. Two-dimensional spinel structured co-based materials for high performance supercapacitors: A critical review. *Chem. Eng. J.* **2020**, *387*, No. 124081.
(86) Mohammadi, H.; Ahmad, Z.; Petru°, M.; Mazlan, S. A.; Johari, M. A. F.; Hatami, H.; Koloor, S. S. R. An insight from nature: Honeycomb pattern in advanced structural design for impact energy absorption. *J. Mater. Res. Technol.* **2023**, *22*, 2862−2887.
(87) Choi, K.; Park, S. H.; Song, Y. M.; Cho, C.; Lee, H. S. Robustly nano-tailored honeycomb structure for high-throughput antireflection polymer films. *J. Mater. Chem.* **2012**, *22*, 17037−17043.
(88) Sivakumar, S.; Venkatesan, A.; Soundhirarajan, P.; Khatiwada, C. P. Thermal, structural, functional, optical and magnetic studies of pure and Ba doped CdO nanoparticles. *Spectrochim. Acta, Part A* **2015**, *151*, 760−772.
(89) Munshi, A.; Prakash, T.; Kumar, E. R. E.; Balamurugan, A.; Habeebullah, T. M.; Bawazeer, T. M.; Abdel-Hafez, S. H.; El-Metwaly, N. M.; Indumathi, T. Comparative investigation of physicochemical properties of cadmium oxide nanoparticles. *Ceram. Int.* **2022**, *48*, 4134−4140.
(90) Din, A.; Khan, S. B.; Khan, M. I.; Asif, S. A. B.; Khan, M. A.; Gul, S.; Akhtar, K.; Asiri, A. M. Cadmium oxide based efficient electrocatalyst for hydrogen peroxide sensing and water oxidation. *J. Mater. Sci: Mater. Electron.* **2017**, *28*, 1092−1100.
(91) Yin, H.; Wen, G. Theoretical prediction and numerical simulation of honeycomb structures with various cell specifications under axial loading. *Int. J. Mech. Mater. Des.* **2011**, *7*, 253−263.
(92) Gao, Y.; Huang, H. Equivalent damper model for honeycomb structures. *Int. J. Mech. Mater. Des.* **2022**, *18*, 475−490.
(93) Reddy, N. K.; Moon, W. J.; Kwon, Y. B.; Jayaram, V.; Arunan, E.; Reddy, K. P. J. Sustainability of carbon nanocomposites under high temperature and pressure. *J. Basic. Appl. Phys.* **2013**, *2*, 78−85.
(94) Sivakumar, A.; Jude Dhas, S. S.; Chakraborty, S.; Kumar, R. S.; Almansour, A. I.; Natarajan, A.; Dhas, S. M. Dynamic shock wave-induced amorphous-to-crystalline switchable phase transition of lithium sulfate. *J. Phys. Chem. C* **2022**, *126*, 3194−3201.

https://doi.org/10.1021/acs.inorgchem.3c03461
Inorg. Chem. 2024, 63, 576−592